HP1 proteins regulate nucleolar structure and function by secluding pericentromeric constitutive heterochromatin

Daniel Ballmer, Mathieu Tardat, Raphael Ortiz, Alexandra Graff-Meyer, Evgeniy A Ozonov, Christel Genoud, Antoine H. F. M. Peters, Grigorios Fanourgakis

Published online 19 December 2022

Nucleic Acids Research, 2023, Vol. 51, No. 1 ***117–143***
https://doi.org/10.1093/nar/gkac1159

HP1 proteins regulate nucleolar structure and function by secluding pericentromeric constitutive heterochromatin

Daniel Ballmer[1,2], Mathieu Tardat[1], Raphael Ortiz[1], Alexandra Graff-Meyer[1], Evgeniy A. Ozonov[1], Christel Genoud[1], Antoine H.F.M. Peters[1,2,*] and Grigorios Fanourgakis[1]

[1]Friedrich Miescher Institute for Biomedical Research, Maulbeerstrasse 66, 4058 Basel, Switzerland and [2]Faculty of Sciences, University of Basel, 4056 Basel, Switzerland

Received June 23, 2022; Revised October 29, 2022; Editorial Decision November 15, 2022; Accepted December 13, 2022

ABSTRACT

Nucleoli are nuclear compartments regulating ribosome biogenesis and cell growth. In embryonic stem cells (ESCs), nucleoli containing transcriptionally active ribosomal genes are spatially separated from pericentromeric satellite repeat sequences packaged in largely repressed constitutive heterochromatin (PCH). To date, mechanisms underlying such nuclear partitioning and the physiological relevance thereof are unknown. Here we show that repressive chromatin at PCH ensures structural integrity and function of nucleoli during cell cycle progression. Loss of heterochromatin proteins HP1α and HP1β causes deformation of PCH, with reduced H3K9 trimethylation (H3K9me3) and HP1γ levels, absence of H4K20me3 and upregulated major satellites expression. Spatially, derepressed PCH aberrantly associates with nucleoli accumulating severe morphological defects during S/G2 cell cycle progression. *Hp1α/β* deficiency reduces cell proliferation, ribosomal RNA biosynthesis and mobility of Nucleophosmin, a major nucleolar component. Nucleolar integrity and function require HP1α/β proteins to be recruited to H3K9me3-marked PCH and their ability to dimerize. Correspondingly, ESCs deficient for both *Suv39h1/2* H3K9 HMTs display similar nucleolar defects. In contrast, *Suv4-20h1/2* mutant ESCs lacking H4K20me3 at PCH do not. *Suv39h1/2* and *Hp1α/β* deficiency-induced nucleolar defects are reminiscent of those defining human ribosomopathy disorders. Our results reveal a novel role for SUV39H/HP1-marked repressive constitutive heterochromatin in regulating integrity, function and physiology of nucleoli.

INTRODUCTION

Nucleoli are the principal sites of ribosome biogenesis in eukaryotic cells and hence are essential for cell viability. They also regulate protein stability in situations of cellular stress (1–6). Mechanisms controlling the formation and function of nucleoli as distinct entities within eukaryotic nuclei are not well understood (7,8).

Nucleoli are formed around genomic nucleolar organizer regions (NORs), consisting of arrays of tandemly repeated rDNA loci. In mouse, rDNA genes are located near centromeric regions on chromosomes 12, 15, 16, 18 and 19, with certain copy number variations existing between strains (9,10). Nucleoli are dynamic, undergoing cycles of disassembly, reassembly and maturation as cells divide and progress through the cell cycle (11–13). During prophase, nucleoli disassemble as RNA polymerase I (RNA pol I)-dependent transcription of rDNA is halted and nucleolar proteins are released from their respective compartments. A subset of transcription factors such as UBF remain, however, associated with NORs throughout mitosis, effectively facilitating the resumption of rDNA transcription upon mitotic exit. In early G1, nucleolar components first accumulate in cytoplasmic nucleolus-derived foci (NDFs) and pre-nucleolar bodies (PNBs) in the nucleoplasm. Next, such components accumulate around active NORs thereby assembling small nucleoli (11). In subsequent S and G2 phases, small nucleoli coalesce into larger round nucleoli accommodating multiple NORs.

*To whom correspondence should be addressed. Fax: +41 616973976; Email: antoine.peters@fmi.ch
Present addresses:
Daniel Ballmer, Department of Biochemistry, University of Oxford, South Parks Rd, Oxford OX1 3QU, United Kingdom.
Mathieu Tardat, Institute of Human Genetics, CNRS UMR 9002, 141 rue de la Cardonille, 34396 Montpellier, France.
Christel Genoud, Electron Microscopy Facility, University of Lausanne, Quartier Sorge-Biophore, 1015 Lausanne, Switzerland.

Nucleoli are partitioned into three distinct subcompartments defined classically by their appearance in electron microscopy and nowadays according to the presence of specific proteins involved in ribosome synthesis (14,15). They comprise the lightly stained fibrillar centers (FCs) that are surrounded by dense fibrillar components (DFCs), both of which are embedded in the granular component (GC). Transcription of rDNA occurs at the interface between the FC and the DFC. Nascent immature pre-rRNAs undergo extensive processing in the DFC and are subjected to pre-ribosome assembly in the GC (15). The compartmentalization of nucleoli is not static but instead is considered to represent a multiphase liquid condensate formed by multivalent interactions between ribosomal RNAs and nucleolar proteins such as Fibrillarin (FBL) and Nucleophosmin (NPM1), key components of DFC and GC layers, respectively (15–18). Homotypic self-interactions of NPM1 and heterotypic interactions of NPM1 with ribosomal RNAs and proteins have been proposed to regulate various kinds of liquid–liquid phase separation (LLPS) processes thereby controlling the spatial directionality of pre-ribosomal particle assembly from the FC/DFC towards the GC and ultimately exit of ribosomal subunits from the nucleolus into the nucleoplasm (16).

Impairments of overall nucleolar shape, subcompartmentalization and integrity have been reported in a heterogenous group of human diseases referred to as ribosomopathies, which are characterized by lowered cellular metabolism and slow growth (7,19–22). Ribosomopathy causing mutations have been identified in various ribosomal proteins such as eL21, uL2, uL5 and uL18, affecting processing of 45S pre-ribosomal transcripts and causing an imbalance between mature 18S and 28S rRNAs. In mutant cells, the nucleolar organization and morphology are dramatically altered, from a generally round into an aberrant amorphic appearance. For example, for uL18, loss of interactions between its Arginine-rich motifs and NPM1 has been proposed to disturb liquid-liquid phase separation processes underlying the formation of the GC (17,23). Similar changes in nucleolar morphology have been reported in undifferentiated embryonic stem cells (ESCs) and E5.5 epiblast embryonic cells deficient for Chd1, a chromatin remodeling enzyme promoting rRNA hyper transcription. In *Chd1* mutant cells, the balance between 18S and 28S is not disturbed arguing that reduced rRNA transcription is sufficient to impair nucleolar structure and function (24).

In naïve undifferentiated ESCs, all rDNA genes are active and nucleoli are large (25), denoting high ribosome biogenesis activity. Upon differentiation, however, several rDNA clusters become transcriptionally repressed and heterochromatinized, acquiring repressive histone H3 lysine9 di- and tri-methylation (H3K9me2/me3), H3K27 tri-methylation (H3K27me3) and DNA methylation (26,27). Differentiation induced heterochromatin formation is triggered by the recruitment of the NoRC complex to rDNA loci in response to differential processing of upstream IGS-rRNA transcripts and the formation of short pRNA molecules (27,28). Exogenous expression of pRNAs is sufficient to establish rRNA gene silencing in ESCs, and to induce differentiation and to some extent a reduction in pluripotency (27). Remarkably, pRNA expression also induces in ESCs a dramatic change in overall nuclear organization. For example, large heterochromatin structures are formed along nucleoli and the nuclear periphery (27), reminiscent of the nuclear organization in differentiated cells (29–31). In mouse, such peri-nucleolar heterochromatic structures contain centromeric and pericentromeric sequences which are comprised of minor and major satellite repeats.

In undifferentiated ESCs, peri- and centromeric satellites are also heterochromatic, yet are clustered solely in multiple large roundish chromocenters. Each of these contain pericentromeric constitutive heterochromatin (PCH) domains of multiple chromosomes. Chromocenters are formed shortly after mitosis and are distributed throughout the nucleus. PCH domains contain 234 bp-long major satellite repeats stretching over several megabases in length (32). Molecularly, PCH is characterized by H3K9me3 that is catalyzed by the SUV39H1/2 enzymes (33,34). This histone modification is bound by chromo domain (CD)-containing proteins such as the SUV39H1/2 enzymes themselves and, importantly, by proteins of the Heterochromatin Protein 1 (HP1) family (35,36) comprising HP1α (CBX5), HP1β (CBX1) and HP1γ (CBX3) in mice. Since HP1 proteins do not only recognize H3K9me3 but also bind to SUV39H1/2 enzymes (37–40), they are thought to constitute a positive feedback loop ensuring effective propagation of H3K9me3 at heterochromatin throughout cell division. HP1 proteins harbor also a chromo shadow domain (CSD), which mediates homo- and heterodimerization between HP1 homologues (41). Dimerization of HP1 proteins is pivotal to their functioning as primary adaptor molecules that effectively organize canonical heterochromatin configuration downstream of the H3K9me3 mark. Firstly, dimerization is necessary for efficient binding of HP1 to H3K9me3-marked chromatin (42). Secondly, the CSD dimer interface enables binding of many heterochromatin factors such as SUV4-20H1/2 and DNMT3A/3B enzymes (43,44) as well as proteins with a PxVxL motif (41,45,46). Thirdly, although DNA mobility measurements revealed that condensed chromocenters display solid-like behavior *in vivo* (47), heterochromatin proteins are dynamically bound at PCH (48–51) and display liquid-like behavior around the solid chromatin scaffold driven in part by dimerization and oligomerization (47,52–56).

From yeast, flies to mice, *Suv39h1/2* orthologs ensure transcriptional repression of satellite sequences and proper chromosome segregation (34,57–59). Even so, chromocenters remain intact in *Suv39h1/2* double null (dn) fibroblasts (34). Additional deficiency of *Setdb1* encoding another H3K9me3 HMT impairs chromocenter integrity, arguing that H3K9me3 is instructive to clustering of PCH regions (60).

Intriguingly, the spatial association of constitutive heterochromatin along the nucleolar periphery appears to be a conserved feature of nuclear organization in many eukaryotes (61–63). To date, it is unknown why and by what means PCH regions are exclusively organized in chromocenters in undifferentiated cells and only become associated with nucleoli upon cellular differentiation. Hence, in this study we investigate the potential role of pericentromeric constitutive heterochromatin in shaping nuclear architecture. To this end we performed loss-of-function studies in mouse

ESCs, focusing on HP1β and HP1α proteins as central organizers within the constitutive heterochromatin pathway. Simultaneous loss of both proteins did not impair chromocenter formation. Instead, it induced frequent associations of PCH domains with nucleoli, and between nucleolar proteins and major satellite transcripts. It further impaired the structural integrity of nucleoli which in part was phenocopied by chemical disruption of weak hydrophobic interactions in nuclei. Our data demonstrate that the unique nuclear organization in undifferentiated ESCs with distinct chromocenters and nucleoli depends on the capacity of HP1 proteins to dimerize and to localize at PCH. Notably, resembling the disruption of nucleolar structure and functions in ribosomopathies, HP1 deletion impaired rRNA biosynthesis and reduced cell proliferation. These data reveal a novel role of HP1-marked constitutive heterochromatin in regulating cellular physiology.

MATERIALS AND METHODS

Constructs

pCAG-Cre:GFP was a kind gift from Connie Cepko (Addgene: pCAG-Cre:GFP). pPy-CAG-CreERT2 plasmid was a kind gift from Joerg Betschinger (FMI, Basel, Switzerland). GFP-tagged NPM1 was a kind gift from Karsten Rippe (German Cancer Research Center (DKFZ) and Bioquant, Heidelberg, Germany). H2B-mCherry was fused to a 3xKSH-ENE sequence to enhance mRNA stability (64). HP1β constructs were described before (36). The HP1β V23M/W170A double point mutant was generated by Gibson assembly (NEB E5510).

Antibodies

For Western blot analysis of histone modifications and associated proteins, the following antibodies were used: monoclonal anti-HP1α (Millipore 05-689, 1:1000), monoclonal anti-HP1β (Serotec MCA1946, 1:1000, CST 8676S, 1:1000), monoclonal anti-HP1γ (Euromedex clone 2MOD-1G6, 1:000), monoclonal anti-b-tubulin (Sigma-Aldrich, 1:000), polyclonal anti-H3K27me3 (Active Motif 39156, 1:2000), polyclonal anti-H3K9me3 (Invitrogen 49-1008, 1:1000), polyclonal anti-H3 (Abcam ab1791, 1:2000), polyclonal anti-H4K20me3 (IMP 0083, 1:2000), polyclonal anti-H4 (Abcam ab10158, 1:4000), polyclonal anti-Myc (Abcam ab9132, 1:1000), monoclonal anti-GFP (Roche 11814460001, 1:1000). Antibodies used for IF stainings and transmission immuno-electron microscopy were: Monoclonal anti-NPM1 (Invitrogen 32–5200, 1:200), monoclonal anti-FBL (CST 2639 1:200), monoclonal anti-UBF1 (Santa Cruz sc-13125, 1:200), polyclonal anti-H3K9me3 (Active motif 39161, 1:1000), monoclonal anti-HP1β (Serotec MCA1946, 1:500, CST 8676S, 1:500), monoclonal anti-HP1α (Millipore 05–689, 1:500), monoclonal anti-HP1γ (Euromedex 2MOD-1G6-AS, 1:1000), polyclonal anti-H4K20me3 (IMP 0083, 1:2000), polyclonal anti-H3K27me3 (Active motif 39156, 1:500), monoclonal anti-H2AK119ub1 (Upstate 05-678, 1:50), polyclonal anti-Myc (Abcam ab9132, 1:500).

Generation of cell lines

To generate constitutive clones, blastocysts from matings of mice homozygous for *Hp1β*$^{F/F}$ or *Hp1β*$^{F/F}$; *Hp1α*$^{F/F}$ (*Cbx1 (Hp1β)* conditionally deficient mice had been generated from ESC clone EPD0027_2_ H02 (EuCOMM) (65) and *Cbx5 (Hp1α)* mouse strain was purchased by EuCOMM Tg(Cbx5tm1a(EUCOMM)Wtsi) were isolated in a single well of a 96-well plate in ESC medium. After 2 days, when blastocysts hatched, they were trypsinized and cells were seeded in the same well for other 2 days. Expanded ESC clones were further tested for their genotype by PCR. Cells from single clones of *Hp1β*$^{F/F}$ or *Hp1β*$^{F/F}$; *Hp1α*$^{F/F}$ were transfected with either pCAG-Cre-GFP or pCAG-GFP as a control. GFP positive cells were sorted by flow cytometry and seeded into 10 cm plates. Individual clones were isolated and expanded. Deletion of *Hp1β* or *Hp1α* floxed alleles in pCAG-Cre-GFP transfected clones was tested by western blotting with appropriate antibodies.

To generate conditional cell lines *Hp1β*$^{F/F}$ and *Hp1β*$^{F/F}$; *Hp1α*$^{F/F}$ ESCs were transfected with a linearized pPy-CAG-CreERT2 plasmid. Cells were selected with blasticidine for at least 2 weeks. Individual clones were expanded and tested by addition of 1μM 4OHT in the medium (H7904, SIGMA). HP1 depletion following addition of 4OHT was confirmed by Western blotting experiments with the appropriate antibodies.

The generation of *Suv39h1/2* control and double null ESCs (WT26, DN57, DN62), *Suv4-20h1/2* double null ESCs (DN1, DN2) and *Adnp1* control and knock-out (KO) ESCs have been described previously (44,66,67).

Cell culture

ESCs were cultured in DMEM medium with 4.5 g/l glucose (Gibco) containing knockout serum replacement (Invitrogen), LIF, penicillin, streptomycin, 2 mM L-glutamine, 0.1 mM β-mercaptoethanol, non-essential amino acids, 1 mM sodium pyruvate (Gibco), in the presence of GSK3β and MEK1 inhibitors (2i) (3 μM CHIR99021, 0.8 μM PD184352, Axon Medchem) at 37°C 5% CO_2. ESCs were initially cultured on a feeder cell layer but adapted to feeder-free conditions for experimental purposes. All experiments were performed on ESCs at a passage between 13 and 22. For assessment of cell proliferation, 250 000 ESCs were seeded per gelatin-coated well of a 6-well culture plate (Corning). After collection on the following day(s), ESCs were counted using a hemocytometer. ESC colonies were imaged on a Leica DMIL microscope equipped with a Leica DFC320 camera and segmented in ImageJ/FIJI using auto-thresholding. Transient transfection of ESCs was performed using Lipofectamine 2000 following the manufacturer's instructions (Invitrogen). Briefly, ∼3 × 10^5 cells were transfected with 4 μl of Lipofectamine 2000 and 3 μg of plasmid DNA prior to seeding onto gelatin-coated dishes and collected ∼1 day later for subsequent experiments. For RT-qPCR and RIP experiments 2 × 10^6 cells were seeded onto a 10 cm dish (Corning) and the amount of transfection reagents was scaled up accordingly.

Flow cytometry

For sorting of ESCs into G1-, S- and G2-enriched populations, ESCs were incubated for 1h in cell culture medium containing Hoechst 33342 (Invitrogen H3570, 1:500) prior to FACS. After harvesting, cells were resuspended in PBS and run on a BD FACSAria III flow cytometer (Becton Dickinson). Cells were gated on FSC-Area vs SSC-Area. Singlets were gated on Hoechst-Area versus Hoechst-Height and sorted into three populations exhibiting low (~2C DNA content), medium and high (~4C DNA content) Hoechst-A signal intensities. For EdU-labeled samples, ESCs were incubated with 10 μM EdU (Santa Cruz Biotechnology) in cell culture medium for 30 min prior to collection. After harvesting, cells were washed with PBS and fixed with 4% paraformaldehyde in PBS for 15 min at room temperature. Next, fixed cells were washed with 1% BSA-PBS and permeabilized with 0.5% triton X-100 in 1% BSA-PBS at room temperature for 15 min. Cells were then pelleted, resuspended in a solution containing PBS with 1 mM $CuSO_4$, 1 μM Alexa Fluor 488 fluorophore-azide (Thermo Fisher, A10266), and 100 mM ascorbic acid (fresh) and incubated for 30 min at room temperature in the dark. Following the labeling reaction, cells were resuspended in 1% BSA–PBS + 0.5% Triton X-100 supplemented with Hoechst 33342 (Invitrogen H3570, 1:1000) and 100 μg/ml RNAse A (Sigma Aldrich). Samples were run on a BD LSRII SORP Analyser (Becton Dickinson). Cells were gated on FSC-Area versus SSC-Area. Singlets were gated on Hoechst-Area versus Hoechst-Height. The positive/negative gates for EdU were gated on a negative control sample, which was not treated with EdU, but otherwise processed as described above. Cell cycle analysis was conducted in FlowJo (Becton Dickinson). For assessment of cell viability, DRAQ7 (BioStatus DR71000, 0.5 μM) was added to the PBS-resuspended cells immediately prior to FACS analysis. Samples were run on a BD LSRII SORP Analyser (Becton Dickinson) and analyzed in FlowJo (Becton Dickinson).

Western blot

For protein blot analysis, 2×10^6 ESCs were washed with PBS and lysed in Laemmli buffer for total protein extraction. For histones extraction, acid extraction was performed according to the Abcam protocol, see: https://www.abcam.com/protocols/histone-extraction-protocol-for-western-blot. Equal amounts of protein (corresponding to ~200 000 cells per sample) were resolved by SDS-PAGE, transferred to a nitrocellulose membrane (Biorad), and probed with a primary antibody overnight at 4°C. Membranes were then incubated with the appropriate HRP-conjugated secondary antibodies (1:10 000, Amersham) and the immunoreactive bands were detected by chemiluminescence. Quantification of band intensities was performed in ImageJ using the commands in the 'gels submenu' (see: https://imagej.nih.gov/ij/docs/menus/analyze.html#gels). To obtain relative protein levels, HP1α or HP1β band intensities were first normalized to the respective b-tubulin loading control and then compared to the value on 'Day 1'.

Transmission (immuno-) electron microscopy

ESCs were seeded onto poly-L-lysine coated Thermanox coverslips. At 50–70% of confluence, ESCs were fixed in 0.1 M HEPES (Sigma-Aldrich, H3375) buffer pH 7.4 containing 2% paraformaldehyde (Electron Microscopy Science, 15700) and 2.5% glutaraldehyde (Electron Microscopy Science, 16200) for half an hour at room temperature and then overnight at 4°C. After three washes in 0.1 M cacodylate (Sigma-Aldrich, C0250) buffer (pH 7.4), ESCs were post-fixed in 1.5% potassium ferrocyanide (Sigma-Aldrich, 60279) and 1% osmium tetroxide (Electron Microscopy Science, 19160) in 0.1 M cacodylate buffer (pH 7.4). After 1 h, the solution was exchanged with 1% osmium in 0.1 M cacodylate buffer (pH 7.4) for 1 h. The cells were then washed in ddH_2O and stained with 1% uranyl acetate in ddH_2O for 20 min. After five washes in ddH_2O and dehydration steps in graded alcohol series, the cells were embedded in EMbed 812 resin (Electron Microscopy Science, 14120) for 12 h and polymerized at 60°C during 24 h. For transmission electron microscopy (TEM) analysis, a region of interest was selected under light microscopy. After trimming, silver/gray thin sections (50 nm thickness) were collected on formvar-coated single-slot copper grids (EMS). After post-staining with 1% uranyl acetate and Reynold's lead citrate (5 min each), images were recorded using a FEI Tecnai Spirit (FEI Company) operated at 120 keV using a side-mounted 2K × 2K CCD camera (Veleta, Olympus).

We performed immuno-EM experiments following a published protocol (68). In brief, ESCs were seeded onto poly-L-lysine coated Thermanox coverslips. At 50–70% of confluence, ESCs were fixed with 2% paraformaldehyde in PBS (Electron Microcopy Scientific 15700). After three washes in PBS buffer, ESCs were permeabilized either with 0.1% Triton-X 100 (Sigma T8787) in PBS or with 0.1% Saponin in PBS (Sigma-Aldrich S0019). The Triton-X 100 permeabilized ESCs group was washed three time in PBS and after 1 h of blocking with 2% BSA (Sigma-Aldrich 05470) in PBS, the ESCs were incubated with anti-FBL or anti-UBF1 primary antibodies in PBS containing 2% BSA for 48 h at 4°C. The Saponin permeabilized ESCs group, as described by (69) were washed three time in PBS containing 0.1% (w/v) Saponin. After 1h of blocking at room temperature in PBS containing 2% BSA (Sigma-Aldrich 05470) and 0.1% (w/v) Saponin, ESCs were incubated with either anti-H3K9me3 primary antibodies or no primary control antibodies (control for unspecific binding) in PBS containing 2% BSA and 0.1% (w/v) Saponin for 1 hour at room temperature. After permeabilization, blocking, washing and incubation with or without primary antibodies, all ESCs groups (Triton-X 100 and Saponin treated groups) were washed two times in PBS and three times with 0.2% BSA-c (Aurion 900.099) in PBS prior immunolabeling with a biotinylated goat anti-rabbit antibody (Jackson ImmunoResearch Europe Ltd 111-066-003) diluted at 1:50 with 0.2% BSAc (and additional 0.1% Saponin – only for Saponin treated ESCs group) in PBS for 3 h at room temperature. Immunostaining was further revealed with a peroxidase-based enzymatic detection system (Vectasatin Elite ABC kit, Vector Laboratories, Burlingame, CA, USA, PK-6100). After washes in TBS (Sigma T5030) ESCs were incubated

for 6 min in 0.02% 3,3'- diaminobenzidine (Sigma-Aldrich D8001) and 0.01% (v/v) H_2O_2 (Sigma-Aldrich H1009) in TBS. The staining reaction was stopped by rinsing the ESCs in TBS. After two washes in bi-distilled water, ESCs were post-fixed in 2% glutaraldehyde for 30 min. After three washes in 100 mM Tris-maleic acid pH 7.4 (Sigma-Aldrich M0375) the DAB reaction was silver-intensified during 10 min at 60°C in the dark by incubation in a solution containing 0.52% hexamethyltetramine (Sigma-Aldrich 398160), 0.04% silver nitrate (Sigma-Aldrich 209139), and 0.04% sodium tetraborate (Sigma-Aldrich 221732) in 100 mM Tris-maleic acid buffer pH 7.4. Then ESCs were rinsed in nanopure H_2O and in PBS and placed in a 0.05% solution of gold chloride (Sigma-Aldrich 520918) for 5 min at room temperature. To wash away unbound silver particles samples were first treated with 3% sodium thiosulfate (Sigma-Aldrich 72049) for 2 min, and then washed three times in bi-distillated water. The samples were then post-fixed with 1.5% osmium tetroxide (EMS 19110) for 30min, rinsed and dehydrated in graded series of ethanol. Samples were further infiltrated in EMbed 812 (Electron Microcopy Scientific 14120) :100% ethanol (1:1 ratio), and then in pure EMbed 812. Finally ESCs were flat embedded and cured overnight at 60°C. Thin sections of 50 nm were cut using a Leica EM UC7 ultramicrotome, and images were recorded at different magnifications (between 8.2 kX and 9.9k× for nucleus overviews) and at 16.5k× magnification for immunolabeling imaging (corresponding to a pixel size of 2.8 nm) using a Tecnai Spirit (FEI, Eindhoven Company) operated at 120 kV using a side-mounted 2K × 2K CCD camera (Veleta, Olympus).

Live cell imaging

Transfected cells were grown on gelatine-coated chambered slides (Ibidi, 81156) and maintained at 37°C and 5% CO_2 in a humidity-controlled environment during acquisition. Nucleolar assembly and dynamics during the cell cycle was imaged for 20 h on a Zeiss AxioObserver 7 inverted microscope equipped with a Yokogawa CSU-W1-T2 spinning disk, a Visitron VS-Homogenizer, a PLAN-APOCHROMAT 100×/1.40 oil objective, Photometrics Prime 95B camera and 488-nm (Obis) and 561-nm (Cobolt) laser lines. Thirty-eight z-axis confocal sections (0.8 μm z-step) of a 1200 × 1200 pixel frame size were acquired every 15 min. The resulting stacks were processed with CARE (70) and assembled into movies using FIJI/ImageJ.

Fluorescence recovery after photobleaching (FRAP)

Transfected cells were grown on gelatine-coated chambered slides (Ibidi, 81156) and maintained at 37°C and 5% CO_2 in a humidity-controlled environment during acquisition. FRAP experiments were conducted using a Zeiss AxioObserver 7 inverted microscope equipped with a Yokogawa CSU-W1-T2 spinning disk, a Visitron VS-Homogenizer, a PLAN-APOCHROMAT 100×/1.40 oil objective, Photometrics Prime 95B camera and a 488-nm laser line (Obis). All devices were piloted with the software Visiview (Visitron GmbH, Puchheim, Germany). The FRAP device (Visitron GmbH, Puchheim, Germany) was mounted on the back port of the scope body and controlled via the VisiFRAP module in the Visiview software (Visitron). Photobleaching was achieved with a 473nm laser line scanned over user-defined regions in the sample thanks to two galvo mirrors in the FRAP device and a long-pass 480nm dichroic mirror (T480lpxr, Chroma, VT, USA) in the microscope body. Circular regions of constant size were bleached and monitored overtime for fluorescence recovery. For each FRAP experiment, a time series of a fixed confocal plane was acquired every 200 ms before and during fluororescence recovery and every 400 ms during later time points. Images were acquired using a frame size of 1200 × 1200 pixels and a pixel depth of 16 bits. Additionally, to calculate the recovery percentage of the bleached foci, a stack (0.8 μm z-step) was taken before and after the time series acquisition.

Immunofluorescence (IF) staining and imaging

ESCs were seeded onto poly-L-lysine coated coverslips or diagnostic slides (Thermo Scientific X1XER308B) and fixed in 4% paraformaldehyde, followed by 1h of blocking and permeabilization in 1% Triton-X 100 in PBS containing 3% BSA. ESCs were then incubated with primary antibodies in PBS-T overnight at 4°C. Prior to application of secondary antibodies ESCs were washed by 3x rinsing in PBS-T followed by a 5 min incubation, and this procedure was repeated 3×. Next, ESCs were incubated with secondary antibodies for 1 h at RT, followed rigorous washing as describe above. Cells were then mounted in Vectashield containing DAPI (Vector H-1200–10). IF staining for Supplementary Figure S1 were imaged on a laser scanning confocal microscope (LSM 700, Zeiss, software: ZEN). One confocal slice through the maximal radius of the cell nuclei was scanned. IF stainings for the rest of the experiments were imaged on a Axio Imager M2 spinning-disk confocal microscope equipped with a Yokogawa CSU W1 Duel camera T2 spinning disk confocal scanning unit, a Visitron VS-Homogenizer, PLAN/APOCHROMAT 63X/1.4 oil objective, a PCO.EDGE4.2M camera, 405-nm (Toptica iBeam), 488-nm (Toptica iBeam), 561-nm (Cobolt Jive) and 639-nm (Toptica iBeam) laser lines. Z-stacks were acquired using a frame size of 2048 × 2048 pixels, a pixel depth of 16 bits, and 0.2 μm z-step. Raw image (STK) files were used as an input for automated segmentation and quantification of IF data.

3D RNA fluorescence in situ hybridization (FISH)

Following IF staining against NPM1 (as described above), RNA-FISH was conducted using Stellaris reagents and according to the manufacturers protocol. Briefly, cells were post-fixed in 3.7% PFA in PBS for 10 min at RT. After washing with PBS, cells were incubated for 5 min in freshly prepared wash buffer A (10% formamide in Wash Buffer A, Biosearch Technologies SMF-WA1-60). A mixture of either forward (5′-GCCATATTTCACGTCCTAAA, 5′-TTTCCACCTTTTTCAGTTTT, 5′-TCCTACAGTGGACATTTCTA, 5′-AGTTTTCTTGCCATATTCCA, 5′-TTTTCAAGTCGTCAAGTGGA) or reverse (5′- AATCCACTTGACGACTTGAA, 5′-AAATGTCCACTGTAGGACGT, 5′-GGACGTGAAATATGGCAAGG, 5′-AC

CTGGAATATGGCGAGAAA) mouse major satellite RNA probes labeled directly by Quasar 570 (Biosearch Technologies) was added to 500 ul hybridization buffer (final working concentration of each probe was 125 nM). Cells were incubated in hybridization buffer containing probe overnight at 37°C in a humidified chamber. Following aspiration of hybridization buffer cells were rinsed in wash buffer A and incubated at 37°C for 30 min in the same buffer. After washing 3 × 5 min in wash buffer B (Biosearch Technologies SMF-WB1-20) at RT, cells were mounted in Vectashield medium containing DAPI (H-1200, Vector Laboratories).

Imaging analysis

Unbiased automatic quantifications of fluorescence intensities shown in Figure 1 and Supplementary Figure S1 were performed from tiled images comprising at least 64 images taken with a 40×/1.3 oil objective. Images were subsequently analyzed with a custom Matlab (MathWorks) script developed in house as described previously (65). Briefly, DAPI staining was classified into chromocenters (high intensity), euchromatin (medium intensity) and background (low intensity outside of nuclei). For each cell, the ratio of mean fluorescence intensity at chromocenters over euchromatic regions was calculated for all channels used. Numerical data was exported into Microsoft Excel and plotted with the Python data visualization libraries Seaborn and Matplotlib. For statistical analysis Mann–Whitney *U* tests were performed.

A custom Python script was used for 3D fluorescence image analysis. Nuclei were first cropped by finding bounding boxes from max intensity projections along x, y and *z*-axis. Then, nuclei masks were obtained by applying Li thresholding on a composite consisting of the DAPI channel summed with blurred NPM1 and FBL channels to fill the holes (71). Nucleoli masks within the nuclei were obtained by Otsu thresholding a composite of the sum of NPM1 and FBL channels minus DAPI (72). Chromocenters were extracted by further Otsu thresholding the DAPI channel within the nuclei mask and excluding the outer boundary (1 μm) (Table 1).

Wrongly or incompletely segmented nuclei (i.e. doublets, nuclei at the edge) were excluded from the final datasets. For the 3D IF data, the image intensities I for the nucleolus mask are normalized with $I' = (I - \mu)/\sigma$ for each channel independently where μ and σ are respectively the mean and standard deviation over the nucleus mask (excluding nucleoli), referred to as Z-score normalization. Plotting and statistical analysis were conducted as described above. Representative IF images shown in figures were deconvoluted using Huygens Remote Manager v3.6 (Scientific Volume Imaging B.V.) and minimal thresholding was applied to adjust for background signal. In the case of 3D imaging data, central slices are depicted in figures.

Analysis of FRAP data was conducted in FIJI/ImageJ. For each FRAP time series, we manually assigned the bleached region as a region of interest (ROI) and calculated the mean intensity of the ROI. We subtracted the obtained minimal intensity from these mean intensities. Fluorescence intensity data were further corrected for background fluorescence and photobleaching resulting from both image acquisition as well as the FRAP laser. To calculate the recovery half-times ($t_{1/2}$), we performed an exponential one-component curve fit based on the formula $y(x) = a(1 - \exp(-bx))$.

For immuno-labeled TEM sections, gold nanoparticles were segmented and counted from 16.5k magnification images that were stitched to cover an entire nucleus. Tile intensities were rescaled to zero median and unit inter-quartile range prior to stitching with the OpenCV stitcher (73). Particles were segmented by applying a watershed algorithm on binary masks generated by adaptive thresholding. Noisy segmentation and debris were removed by area filtering.

For nucleoli and chromocenters segmentation on TEM sections, a deep learning U-net like fully convolutional network (74) was trained with cross-entropy loss on manual annotations to predict nucleus vs background classes. Separate networks were trained in similar fashion to predict either 'background vs. nucleoli' or 'background vs. nucleoli vs. chromocenters' classes for the TEM and the H3K9me3-immune-labelled TEM datasets, respectively. Nuclei overviews were processed at their native resolution (2048 × 2048 px^2) while stitched images were down-scaled and padded to 2048 × 2048 px^2 prior to processing. Morphological properties extracted from binary masks were corrected for variations in magnification. 'PCH-Nucleolus contact' shown in Figure 3G was calculated as the fraction of nucleoli borders that are in direct contact with chromocenter borders. 'Intra-nucleolar H3K9me3 particles' represents the fraction of total segmented H3K9me3 immuno nano-particles detected within nucleoli'.

RNA-seq

Cells were harvested and RNA was isolated with the RNeasy mini kit (Qiagen) according to the manufacturer's protocol. RNA was further treated with Turbo DNase (AMbion) to remove residual DNA. rRNA-depleted sequencing libraries were prepared with ScriptSeq v2 RNA-Seq Library Prep Kit (Illumina) and sequencing was performed on HiSeq200 with 50 bp paired end reads according to manufacturer instructions. Alignment of RNA-seq samples was done using STAR, allowing multimappers with up to 300 matches in the genome and choosing positions for multimappers randomly. Read counting for genes was done using QuasR with no restriction for mapping quality (i.e. multimappers included). Genes which had log2(RPKM) value less than 1 in all samples were removed from the analysis. After filtering non-expressed genes, 17 968 genes were analysed in total. Differentially expressed genes were identified using edgeR package with cutoffs FDR ≤0.05 and FoldChange ≥ 1. Multiplicity correction was performed by applying the Benjamini-Hochberg method on the *P*-values, to control the false discovery rate (FDR). Statistical significance of differential expression was estimated using quasi-likelihood test.

Chromatin Immunoprecipitation (ChIP)

2 × 10^6 ESCs were incubated in 200 ul of Lysis Buffer (15 mM Tris–HCl (pH 7.5), 300 mM Sucrose, 60 mM KCl,

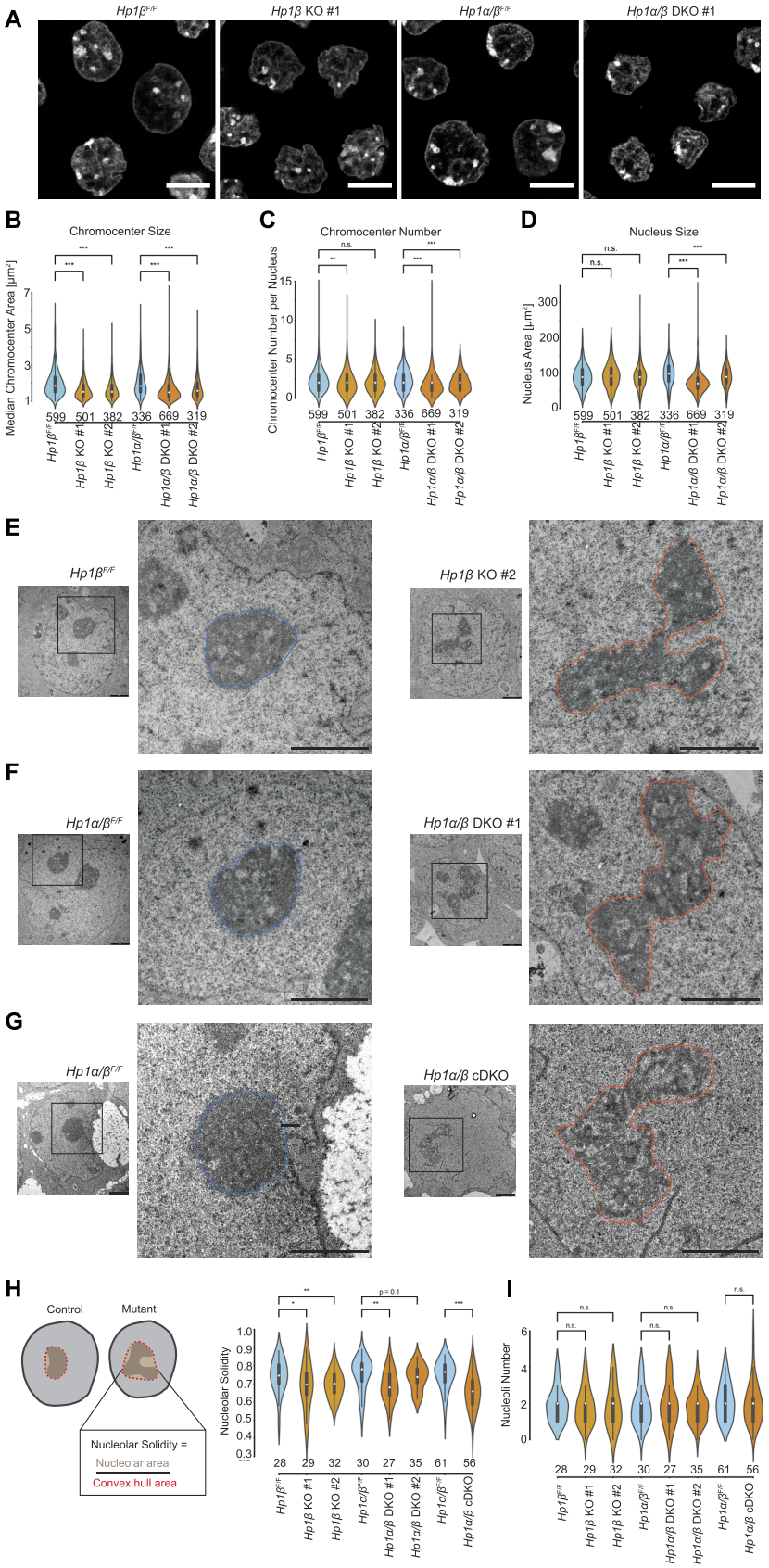

Figure 1. Morphological alterations to nuclei and nucleoli in *Hp1α/β* deficient ESCs. (**A**) Representative DAPI staining of nuclei from control, *Hp1β*-KO and *Hp1α/β*-DKO ESCs. Scale bars = 10 μm. (**B–D**) Violin plots showing the area of chromocenters (B), number of chromocenters (C) and the area

15 mM NaCl, 5 mM $MgCl_2$, 0.1 mM EGTA, 0.25% NP-40, 0.5% DOC, 0.5 mM DTT, 1× Protease Inhibitor Cocktail) for 10 min on ice. 200 ul of MNase Buffer (85 mM Tris–HCl (pH 7.5), 300 mM sucrose, 3 mM $MgCl_2$, 5 mM $CaCl_2$, 6 U/ul MNase) were added to the lysate and incubated for 10 min at 25°C. Reaction was stopped by adding 8 ul 0.5M EDTA and incubating on ice for 10 min. Lysate was centrifuged at 16 000g for 10 min at 4°C, supernatant was transferred to new tubes and 800 ul of ChIP buffer (50 mM Tris–HCl (pH 7.5), 300 mM sucrose, 30 mM KCl, 15 mM NaCl, 4 mM $MgCl_2$, 2.5 mM $CaCl_2$, 0.05 mM EGTA, 0.125% NP-40, 0.25% DOC, 0.25 mM DTT, 1× Protease Inhibitor Cocktail). DNA concentration was quantified by NanDrop and chromatin corresponding to 30 ug of DNA was incubated with 20 ul equilibrated protein G Dynabeads in a final volume of 500ul adjusted with ChIP buffer for 1 h at 4°C on the rotator. Samples were placed on the magnetic rack and the supernatant was transferred to new tubes. 5% of the chromatin was aliquoted to serve as input while the rest of the sample was incubated with 2 ug/ml a-H3K9me3 antibody at 4°C on the rotator overnight. Next day 20 ul of equilibrated protein G Dynabeads were added to each sample for 4 h at 4°C on the rotator. After the incubation, the Dynabeads were separated from the sample using a magnetic stand. Dynabeads were washed 3 times with Low Salt Buffer (10 mM Tris/Cl pH 7.5, 250 mM NaCl, 0.5 mM EDTA 0.1% Triton X-100, 0.05% SDS, 1× Protease Inhibitor cocktail) and 3 times with High Salt Buffer (10 mM Tris–HCl pH 7.5, 500 mM NaCl, 0.5 mM EDTA 0.1% Triton X-100, 0.05% SDS, 1× Protease Inhibitor cocktail). Afterwards the Dynabeads were resuspended in 40 Elution Buffer (100 mM sodium bicarbonate, 1% SDS) and incubated for 90 min at 65°C. Dynabeads were discarded and immunoprecipitated DNA was purified by adding 2 volume of Ampure XP Beads (Beckman Coulter), following the manufacturer's instructions and eluted in 25 ul of nuclease free H_2O.

RNA Immunoprecipitation (RIP)

2×10^6 ESCs were crosslinking in 0.5% PFA at room temperature for 10 min. Crosslinking was quenched by the addition of 0.1 M glycine final concentration and cells were centrifuged at 500g for 10 min. After 2 washes with PBS, the cell pellet was snap frozen in liquid nitrogen, then resuspended in 200 ul of Lysis Buffer (10 mM Tris–HCl pH 7.5, 150 mM NaCl, 0.5 mM EDTA, 1% Triton X-100, 0.5% SDS, 1% sodium deoxycholate, 1× Protease Inhibitor cocktail, 40 U/ml RNAsin) and incubated on ice for 10 min. Cell lysate was sonicated using a Bioraptor for 10 cycles (30 s ON, 30 s OFF, high output) and centrifuged at 16 000g for 10 min at 4°C. The supernatant was diluted with 800 ul Dilution Buffer (10 mM Tris–HCl pH 7.5, 150 mM NaCl, 0.5 mM EDTA, 1× Protease Inhibitor cocktail, 40 U/ml RNAsin). 50 ul of the supernatant was aliquoted to serve as the input. 25 ul of equilibrated GFP-Trap Dynabeads (Chromotek) was added to the sample and incubated for 1 h at 4°C on the rotator. After the incubation, the Dynabeads were separated from the sample using a magnetic stand. Dynabeads were washed 3 times with Low Salt Buffer (10 mM Tris–HCl pH 7.5, 250 mM NaCl, 0.5 mM EDTA 0.1% Triton X-100, 0.05% SDS, 1× Protease Inhibitor cocktail) and 3 times with High Salt Buffer (10 mM Tris–HCl pH 7.5, 500 mM NaCl, 0.5 mM EDTA 0.1% Triton X-100, 0.05% SDS, 1× Protease Inhibitor cocktail). Afterwards the Dynabeads were resuspended in 100 ul Elution Buffer (10 mM EDTA, 1% SDS, 100 mM Tris–HCl pH 7.5, 200 mM NaCl, 1 mg/ml Proteinase K) and incubated for 15 min at 42°C followed by 1 h at 65°C. Dynabeads were discarded and 300 ul of Trizol was added to each sample. Subsequently, RNA isolation, reverse transcription and real time PCR were performed as described later.

Reverse transcription

RNA isolation was performed using Direct-zol RNA MiniPrep (Zymo Research, R2050), according to the manufacturer's instructions. RNA was subjected to an additional round of DNAse treatment in solution to remove residual contaminating genomic DNA, followed by a clean-up step. As a quality control, the purified RNA was run on an Agilent 2100 Bioanalyzer. Reverse transcription was performed with SuperScript III Reverse Transcriptase (Invitrogen, 18080085) according to the manufacturer's instructions, using random hexamer primers (Thermo Fisher, SO142).

Real time PCR

Amplification was carried out using SYBR Green PCR Master Mix (Thermo Fisher, 4309155) and 500 nmol of the following primers: For RNA amount experiments: 28S rRNA (F: 5′- GCGACCTCAGATCAGACGTGG, R: 5′-CTGTTCACTCGCCGTTACTGAG), 5′-ETS (1) (F: 5′-CTCTTGTTCTGTGTCTGCC, R: 5′- GCCCGC TGGCAGAACGAGAAG), 5′-ETS (2) (F: 5′-GTCTT CTGGTTTCCCTGTGTG, R: 5′- GCTAGAGAAGGA AACTTTCTCACTG), ITS2 (F: 5′- GAGAACGGAG AGAGGTGGTATC, R: 5′- AGAAGCGGAGACGAAG AAGAG), IGS (F: 5′-GCAGACCGAGTTGCTGTAC,

←

of nuclei (D) based on the DAPI staining of cells for the indicated genotypes. (**E**) Representative transmission electron micrographs showing nuclear and nucleolar morphology of a control ($Hp1\beta^{F/F}$) and constitutive $Hp1\beta$-KO ESC clone number 2. Scale bars = 2 μm. Nucleoli have been highlighted in higher magnification panels. (**F**) Representative transmission electron micrographs showing nuclear and nucleolar morphology of a control ($Hp1\alpha^{F/F}$; $Hp1\beta^{F/F}$) and constitutive $Hp1\alpha/\beta$-DKO ESC clone number 1. Scale bars = 2 μm. Nucleoli have been highlighted in higher magnification panels. (**G**) Representative transmission electron micrographs showing nuclear and nucleolar morphology of a control and a conditional $Hp1\alpha/\beta$-cDKO ESC ($Hp1\alpha^{F/F}$; $Hp1\beta^{F/F}$; Cre-ERT2 ESCs after 4 days of mock EtOH or 4-OHT treatment, respectively). Scale bars = 2 μm. Nucleoli have been highlighted in higher magnification panels. (**H**) Left panel: Schematic representation depicting measurement of nucleolus solidity, which is computed as the ratio of the area of a nucleolus to the area of its convex hull. Right panel: violin plots showing the quantification of nucleolar solidity for the indicated genotypes. (**I**) Violin plots showing the quantification of nucleoli number per nucleus for the indicated genotypes. Sample sizes are indicated below each violin. * $P < 0.05$, ** $P \leq 0.01$, *** $P \leq 0.001$ (Mann–Whitney U).

Table 1. Parameters used to create fluorescent composite images from normalized NPM1, FBL and DAPI channels

	Channel smoothing size	Channel weight	Threshold method
Nuclei	99, 99, 5	0.5, 0.5, 1	Li
Nucleoli	1, 19, 19	5, 5, –1	Otsu
Chromocenters	0, 0, 0	0, 0, 1	Otsu

R: 5′- GGGTAGGACTTAAGCCTT) on an ABI StepOnePlus Real-Time PCR System (Applied Biosystems). Relative rRNA levels were determined by normalizing to *b-actin* (F: 5′- CCAACTGGGACGACATGGAG, R: 5′-CTCGTAGATGGGCACAGTGTG). For RIP experiments: 18S rRNA(F: 5′-GTAACCCGTTGAACCCCATT, R: 5′-CCATCCAATCGGTAGTAGCG), Major Satellite (F: 5′-GACGACTTGAAAAATGACGAAATC, R: 5′-CATATTCCAGGTCCTTCAGTGTGC). For ChIP experiments: Major Satellite and 28S rRNA as before, β- actin promoter (F: 5′-GCAGGCCTAGTAACCGAGACA, R: 5′-AGTTTTGGCGATGGGTGCT), rDNA enhancer (F: 5′-GAAGCCCTCTTGTCCCCGTC, R: 5′-GATCCAAAGCTCCAGCTGAC), rDNA promoter (F: 5′-GACCAGTTGTTCCTTTGAGG, R: 5′- ACCTATCTCCAGGTCCAATAG). Numerical data was analyzed in Microsoft Excel and plotted with the Python data visualization library Seaborn/Matplotlib. Statistical significance (*P*-values) was calculated using a two-sided, unpaired t-test.

RESULTS

Deficiency for HP1α/β reduces HP1γ and H4K20me3 levels at pericentromeric heterochromatin

In mouse cells, HP1α and HP1β are predominantly localized at constitutive heterochromatic regions of the genome, whereas HP1γ resides both in euchromatic as well as heterochromatic compartments (75–78). To study the function of the main constitutive heterochromatic HP1 paralogues in nuclear organization, we derived multiple ESC lines from mouse blastocyst embryos that are either homozygously floxed for *Hp1β* alleles ($Hp1\beta^{F/F}$) only or additionally for *Hp1α* alleles as well ($Hp1\alpha^{F/F};Hp1\beta^{F/F}$). We transiently expressed Cre recombinase and established two independent *Hp1β* single knock-out (*Hp1β*-KO #1 and #2) and two *Hp1α* and *Hp1β* double knock-out (*Hp1α/β*-DKO #1 and #2) clonal ESC lines (Supplementary Figure S1A and Material & Methods). In floxed control ESCs, immunofluorescence (IF) staining showed that all three paralogs were enriched at PCH-chromocenters relative to surrounding euchromatin, as characterized by bright versus moderate staining of 4,6-diamidino-2-phenylindole (DAPI) respectively. The proteins were non-detectable in DAPI-dim nucleoli (Supplementary Figures S1B, S1C, S1D). In mouse cells, chromocenters can be easily identified based on bright DAPI signals, given its preferential binding to AT-rich major satellite repeat sequences (Figure 1A) (79).

Beside the anticipated absence of HP1β protein in *Hp1β*-KO ESCs (Supplementary Figure S1B, S1E), we observed a significant reduction in HP1α and HP1γ levels at PCH without measuring a reduction in corresponding total cellular protein levels by Western blot analyses (Supplementary Figures S1C, S1D, S1E). In *Hp1α/β*-DKO ESCs, HP1α and HP1β proteins were absent (Supplementary Figures S1B, S1C, S1E). HP1γ localization at PCH was also reduced in *Hp1α/β*-DKO ESCs as in single *Hp1β*-KO ESCs (Supplementary Figure S1D). These data show interdependencies between HP1 paralogs in their recruitment to constitutive heterochromatin in ESCs, as observed in more differentiated cells (80,81).

H3K9me3 intensities at PCH were variably affected in different stable single and double mutant ESC clones (Supplementary Figures S1G, S1I). Importantly, H3K27me3 enrichment at PCH was slightly reduced in all mutant lines while H2AK119ub1 levels remained unaffected (Supplementary Figures S1H, S1I). This contrasts to *Suv39h1/2* dn ESCs in which PCH acquires H3K27me3 in absence of H3K9me3 (82).

Furthermore, the level of H4K20-trimethylation, catalyzed by the HP1-interacting enzymes SUV4-20H1 and SUV4-20H2 (83), was greatly decreased at PCH in both *Hp1β*-KO and *Hp1α/β*-DKO ESCs (Supplementary Figures S1F, S1I). Yet, unlike in *Suv4-20h1/2* deficient MEFs, we did not observe scattering of chromocenters (43). Together, these observations support the notion that HP1 paralogues function at PCH upstream of the SUV4-20H1/H2 enzymes and downstream of SUV39H1/2-mediated H3K9me3 (81,83,84).

Deficiency for HP1α/β perturbs nucleolar morphology

Intriguingly, the number of chromocenters was moderately decreased and their sizes majorly reduced in both *Hp1β*-KO and *Hp1α/β*-DKO ESCs (Figure 1A–1C). In addition, *Hp1α/β*-DKO ESCs exhibited reduced nuclear sizes (Figure 1D), suggesting a role for HP1 proteins in regulating nuclear architecture. To investigate such role in more detail, we performed transmission electron microscopy (TEM) on ultra-thin sections of ESC colonies. In control ESCs, chromatin appeared homogeneously in granularity and devoid of electron-dense structures, reminiscent of a de-compacted chromatin configuration characteristic of the pluripotent state (85,86). Most prominently visible nuclear substructures were nucleoli, which appeared as rounded, highly contrasted compartments (Figure 1E–G, Supplementary Figure S1J, S1K). Remarkably, we observed a severe disruption of the typical roundish nucleolar morphology in *Hp1β*-KO and *Hp1α/β*-DKO ESCs, that instead was characterized by variable amorphous grainy appearances with extensive curvatures (Figure 1E, 1F, Supplementary Figure S1J, S1K). To enable an unbiased and quantitative analysis of nucleoli structures, we segmented nucleoli in 2D using a machine learning algorithm and measured the nucleolus solidity, calculated as the ratio of nucleolus area to the area of the smallest convex shape enclosing the nucleolus area, referred to as the convex hull (Figure 1H, Materials and Methods). Notably, nucleolar solidity was high in control cells and reduced to variable degrees in HP1 single and double deficient clones, confirming a general loss of spherically shaped nucleoli in mutant cells (Figure 1H).

To exclude that the atypical non-spherical morphology observed in *Hp1α/β* stably deficient cells resulted indi-

rectly from adaptation to *in vitro* culture conditions, we derived $Hp1\alpha^{F/F}$; $Hp1\beta^{F/F}$ ESC lines stably expressing CreERT2 recombinase, thereby allowing rapid conditional deficiency upon 4-hydroxytamoxifen (4-OHT) administration (*Hp1α/β*-cDKO). 4-OHT treatment resulted in a ∼10-fold depletion of HP1α/β proteins after two days, and complete loss of both proteins after four days of treatment (Supplementary Figures S2A, S2B). Importantly, ESCs exhibited 4 days upon 4-OHT induced co-depletion of HP1α and HP1β severe nucleolar defects comparable to their constitutive counterparts as observed by TEM (Figure 1G, H). The number of nucleoli per cell was not altered in *Hp1β*-KO nor *Hp1α/β*-(c)DKO ESCs (Figure 1I). Together, these data demonstrate that HP1α/β proteins regulate nucleolar morphology in ESCs.

Perturbations in nucleolar morphology unfold in a cell cycle dependent manner upon loss of HP1α/β

Since nucleoli assemble during cell cycle progression, we aimed at monitoring the cell cycle dependence of altered nucleolar morphology formation in *Hp1α/β*-DKO ESCs. Towards this, we first expressed GFP-NPM1 and histone H2B-mCherry fusion proteins to mark the GC of nucleoli and overall chromatin, respectively, and performed live cell microscopy. Upon exit of mitosis, many small nucleoli in control cells coalesced within 2–3 h into larger mature spherical nucleolar structures that subsequently underwent dynamic fusion and fission events throughout the remaining interphase. In contrast, small nucleoli in DKO cells merged into larger amorphously shaped nucleoli that maintained their atypical shapes throughout the cell cycle despite ongoing fusion and fission events (Figure 2A and Movies S1, S2).

On top, we observed a reduced mobility of GFP-NPM1 proteins in mutant cells in Fluorescence Recovery after Photobleaching (FRAP) experiments (Figure 2B, 2C). Upon bleaching, the half recovery time of nucleolar GFP-NPM1 was 1.5-fold elevated and its immobile fraction was doubled in *Hp1α/β*-DKO compared to control ESCs (Figure 2C, 2D), arguing for structural changes underlying the morphological alterations of nucleoli.

To further investigate the temporal aspects of the nucleolar defects observed in single and double mutant ESCs, we sorted cells into G1, S and G2 phase enriched populations based on their DNA content (Supplementary Figure S3A) and measured protein levels for major structural components of nucleoli by Western blot. Cellular levels of NPM1 and the rRNA processing enzyme FBL were not substantially altered upon loss of HP1α/β (Supplementary Figure S3B). Next we co-stained for NPM1 and FBL, labeling the GC and DFC respectively, thereby enabling a delineation of the intra-nucleolar organization. In control ESCs, the size of nucleoli increased during cell cycle progression (Figure 2E, 2F). G1 nuclei often harbored numerous nucleoli as well as dispersed NPM1 or FBL-positive puncta, corresponding to pre-nucleolar bodies (PNBs). In S and G2 phase nuclei, PNBs were absent and large nucleoli were spherical and comprised of a layer of NPM1 surrounding a granulated FBL-positive interior (Figure 2E). Intriguingly, in *Hp1α/β*-DKO ESCs, PNBs and small nucleoli assembled normally in early G1. Nucleoli, however, failed to subsequently match the volume and spherical shape of their control counterparts, resulting in smaller, irregular structures during mid to late interphase. Moreover, NPM1 and FBL partly co-localized in mutant cells (Figure 2E). Thus, while nucleolar solidity was not affected at G1, it was significantly reduced at S and G2 in *Hp1α/β*-DKO cells compared to controls (Figure 2G). Conditional depletion of *Hp1α/β* also resulted in a marked decrease in volume and solidity of nucleoli (Supplementary Figures S3C, S3D, S3E). In single *Hp1β*-KO ESCs we detected moderate nucleolar defects (Supplementary Figures S3F, S3G, S3H).

Finally, we investigated the organization of the FCs relative to the DFCs by probing the spatial distribution of the Pol I transcription factor UBF1 and FBL using IF and immuno-TEM approaches (Figure 2H, 2L, 2M). UBF1 was detected as discrete fluorescent foci in nucleoli, that were largely excluded from FBL-positive domains (Figure 2H). In *Hp1α/β*-DKO ESCs we detected a moderate increase in the number of UBF1 foci per nucleolus (Figure 2I) and closer association of UBF1 foci to the nucleolar periphery (Figure 2J, 2M) suggesting scattering and mislocalization of this subnucleolar compartment. Nonetheless, we didn't observe significant changes in FBL labeling over UBF1 foci (Figure 2K). Immunolabeling of TEM samples showed that FBL was present at more darkly stained DFC compartments and excluded from the pale stained FC compartments in *Hp1α/β*-DKO as in control ESCs (Figure 2L), arguing that these subnucleolar compartments remain separate. Together, these data show that HP1α and HP1β control the maturation of nucleolar organization during cell cycle progression.

HP1 proteins prevent aberrant association between PCH and nucleoli

Given the prominent role of HP1α/β proteins in heterochromatin formation at PCH (Figure 1) (35,36,41–44,46), we investigated the role of PCH in nucleolar deformation in mutant cells. Time lapse imaging of control and *Hp1α/β*-DKO ESCs expressing H2b-mCherry and GFP-NPM1 revealed dynamic invasions of chromatin into nucleoli of mutant but not control cells (Figure 3A, Movies S1–4). IF analysis of cell cycle sorted constitutive and conditionally deficient *Hp1α/β* ESCs showed DAPI-bright chromocenter foci co-localizing with and/or being enclosed within NPM1/FBL-positive regions (Supplementary Figures S4A, S4B, S4C, Movies S5 and S6). To quantify the spatial interactions between PCH and nucleoli, we applied 3D segmentation on DAPI-bright PCH foci and segmented nucleoli. We measured two 'interaction parameters': (i) 'intranucleolar DAPI' as the *z*-score normalized intensity of DAPI inside segmented nucleoli and (ii) 'chromocenter-nucleolus intersection' as the volume of intersection between segmented chromocenters and nucleolar masks normalized to total chromocenter volume. These quantifications unambiguously show increased interactions between chromocenters and nucleoli in both straight and conditional *Hp1α/β* double deficient ESCs, in particular during S and G2 phases coinciding temporally with the observed nucleolar defects (Figure 3B, 3C, Supplementary Figure S4D,

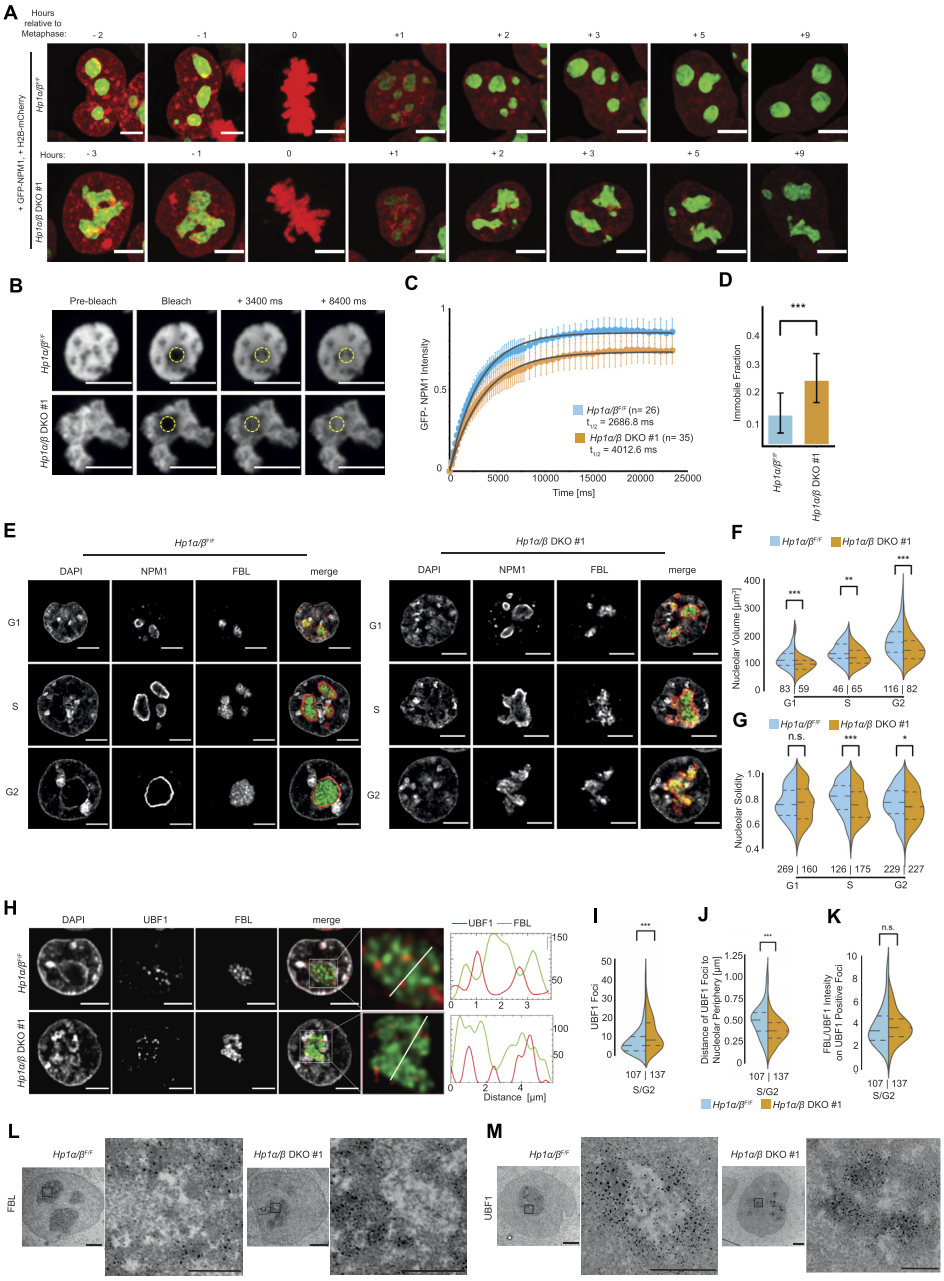

Figure 2. Cell cycle dynamics and structural organization of nucleoli in control and *Hp1α/β* deficient ESCs. (**A**) Representative live imaging of GFP-NPM1 and H2B-mCherry transfected control ($Hp1\alpha^{F/F}$; $Hp1\beta^{F/F}$) and *Hp1α/β*-DKO ESCs. Maximum projection of multiple confocal z-stacks is shown. Time is presented relative to the frame when the metaphase plate is observed. Scale bars = 5 μm. (**B**) Representative fluorescence microscopy images at indicated timepoints during FRAP of GFP-NPM1 within a region of interest in a control ($HP1\alpha^{F/F}$; $HP1\beta^{F/F}$) and *Hp1α/β*-DKO ESC nucleolus. Scale bars = 5 μm. (**C**) Normalized and averaged FRAP curves, corrected for photobleaching, for GFP-NPM1 within control and *Hp1α/β*-DKO ESC nucleoli. The exponential fits used to calculate $t_{1/2}$ are shown in black. (**D**) Bar plots representing the GFP-NPM1 immobile fraction extracted from FRAP curves shown in (C). (**E**) Representative IF staining against NPM1 and FBL in G1, S and G2 of control ($Hp1\alpha^{F/F}$; $Hp1\beta^{F/F}$) and *Hp1α/β*-DKO ESCs. DNA was stained with DAPI. Central slices of confocal z-stacks are shown. Scale bars = 5 μm. (**F**) Violin plots showing the quantification of nucleolar volume in G1, S and G2 of control ($Hp1\alpha^{F/F}$; $Hp1\beta^{F/F}$) and *Hp1α/β*-DKO ESCs from (E). (**G**) Violin plots showing the quantification of nucleolar solidity in G1, S and G2 of control ($Hp1\alpha^{F/F}$; $Hp1\beta^{F/F}$) and *Hp1α/β*-DKO ESCs from (E). (**H**) Left panels: Representative IF staining against UBF and FBL. Scale bars = 5 μm. Right panels: Line scans depict co-localization of UBF1 (red) and FBL (green) signals. DNA was stained with DAPI. (**I**) Violin plot showing the quantification of UBF1 foci inside the 3D segmented nucleolus of control ($Hp1\alpha^{F/F}$; $Hp1\beta^{F/F}$) and *Hp1α/β*-DKO ESCs from (H). (**J**) Violin plot showing the distance of UBF1 foci from the segmented nucleolus periphery of control ($Hp1\alpha^{F/F}$; $Hp1\beta^{F/F}$) and *Hp1α/β*-DKO ESCs from (H). (**K**) Violin plots showing the fluorescence intensity ratio of FBL to UBF1 at the segmented UBF1 foci inside the 3D segmented nucleolus of control ($Hp1\alpha^{F/F}$; $Hp1\beta^{F/F}$) and *Hp1α/β*-DKO ESCs from (H). (**L**) Representative anti-FBL (FBL) immuno-TEM micrographs in a control ($Hp1\alpha^{F/F}$; $Hp1\beta^{F/F}$) and an *Hp1α/β*-DKO ESC. Dark puncta in the zoomed in panels represent the immune-reactive sites. (**M**) Representative anti-UBF1 immuno-TEM micrographs highlighting FC organization and localization in a control ($Hp1\alpha^{F/F}$; $Hp1\beta^{F/F}$) and an *Hp1α/β*-DKO ESC. Dark puncta in the zoomed in panels represent the immune-reactive sites. Scale bars = 2 μm. Sample sizes are indicated below each violin. * $P < 0.05$, ** $P \leq 0.01$, *** $P \leq 0.001$ (Mann–Whitney *U* test).

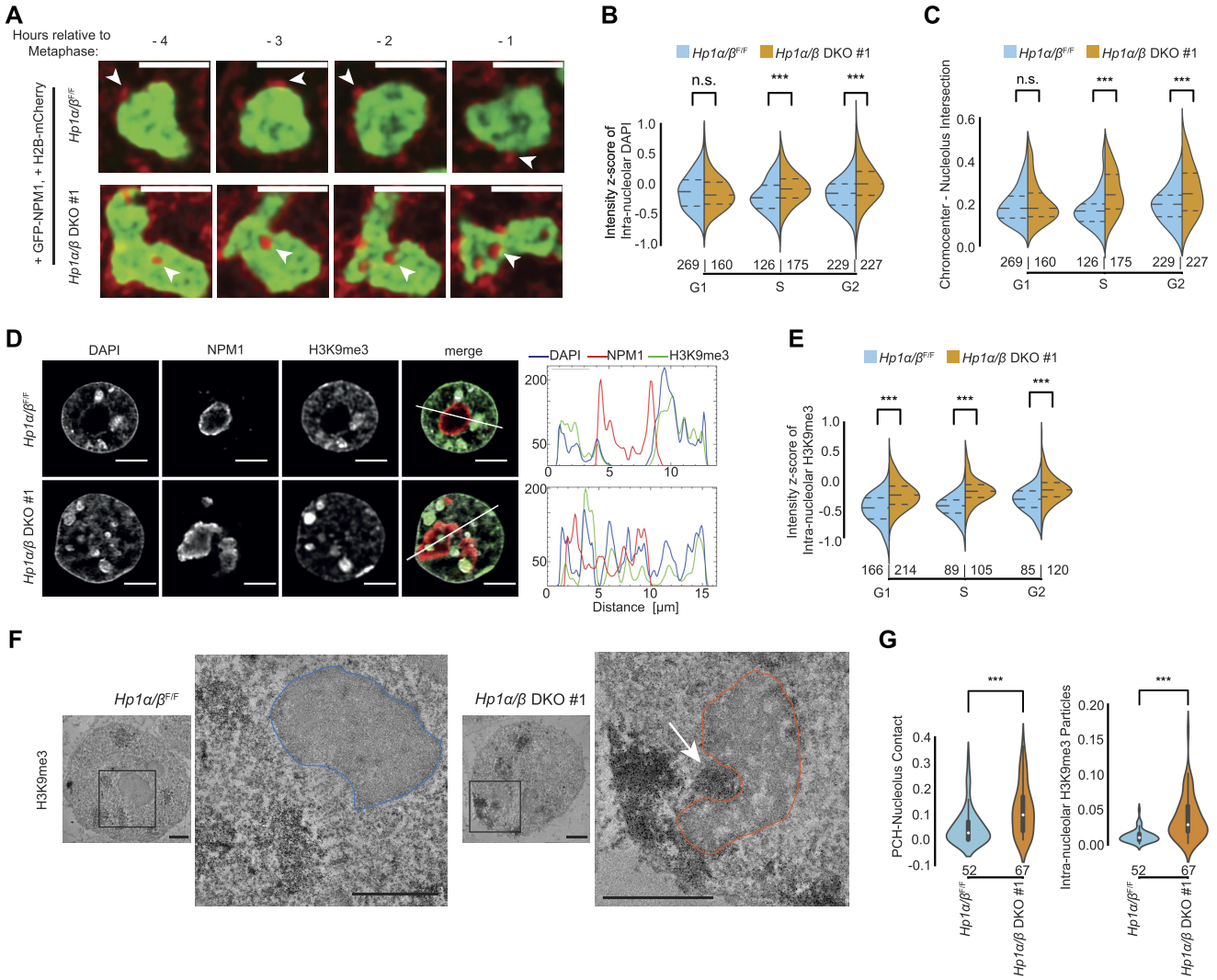

Figure 3. Aberrant associations between nucleoli and pericentromeric heterochromatin in *Hp1α/β* deficient ESCs. (**A**) Representative nucleoli live imaging of GFP-NPM1 and H2B-mCherry transfected control ($Hp1\alpha^{F/F}$; $Hp1\beta^{F/F}$) and *Hp1α/β*-DKO ESCs. Single central slices of confocal z-stacks are shown. Time is presented relative to the frame when the metaphase plate is observed. Arrow heads indicate chromatin (H2B-mCherry bright puncta) associations with nucleolus (GFP-NPM1 positive regions). Scale bars = 5 µm. (**B, C**) Violin plots showing the quantification of intra-nucleolar DAPI (B) and chromocenter-nucleolus intersection (C) in G1, S and G2 of control ($Hp1\alpha^{F/F}$; $Hp1\beta^{F/F}$) and *Hp1α/β*-DKO ESCs from (Figure 2E and Supplementary Figure S4A). (**D**) Left panels: Representative IF staining against NPM1 and H3K9me3 of control ($Hp1\alpha^{F/F}$; $Hp1\beta^{F/F}$) and *Hp1α/β*-DKO ESCs in S phase. DNA was stained with DAPI. Central slices of confocal z-stacks are shown. Scale bars = 5 µm. Right panels: Line scans indicate (co)localization between DAPI (blue), NPM1 (red) and H3K9me3 (green) signals. (**E**) Violin plots showing the quantification of intra-nucleolar H3K9me3 in G1, S and G2 of control ($Hp1\alpha^{F/F}$; $Hp1\beta^{F/F}$) and *Hp1α/β*-DKO ESCs (from D). (**F**) Representative anti-H3K9me3 Immuno-TEM micrographs highlighting aberrant chromocenter-nucleolus associations in a control ($Hp1\alpha^{F/F}$; $Hp1\beta^{F/F}$) and an *Hp1α/β*-DKO ESC. Nucleoli edges have been highlighted in the zoomed in panels. Dark puncta represent the H3K9me3 immune-reactive sites and arrow indicates H3K9me3-positive material invading the nucleolus. Scale bars = 2 µm. (**G**) Violin plots showing the quantification of chromocenter-nucleolus contacts (left panel) and the intra-nucleolar H3K9me3 particles in control ($Hp1\alpha^{F/F}$; $Hp1\beta^{F/F}$) and *Hp1α/β*-DKO ESCs (from F). Sample sizes are indicated below each violin. * $P < 0.05$, ** $P \leq 0.01$, *** $P \leq 0.001$ (Mann–Whitney *U*-test).

S4E). Double staining for H3K9me3 and NPM1 confirmed increased colocalization of H3K9me3 and DAPI-labeled chromocenters and NPM1-demarcated nucleolar areas in *HP1α/β*-DKO versus control ESCs (Figure 3D, 3E).

To validate this finding at high resolution, we performed immuno-TEM for H3K9me3 and segmented nucleoli and PCH regions, the latter characterized by high concentrations of anti-H3K9me3 immuno-staining. We calculated the fraction of PCH pixels in direct contact with the nucleolar periphery as a measure of interactions between these domains. In control ESCs, nucleoli and PCH did not intermix and persisted as clearly separated substructures (Figure 3F, 3G). *Hp1α/β*-DKO ESCs exhibited extensive contacts between nucleoli and PCH, with the latter being frequently accommodated within nucleolar cavities (Figure 3F, 3G). Together, we conclude that HP1α/β proteins restrain chromocenters from dynamically intruding into nucleolar domains of ESCs.

Chemical perturbation of weak hydrophobic interactions partially phenocopies nuclear disorganization in HP1 deficient ESCs

Liquid-liquid phase separation (LLPS) mechanisms have been implicated in the formation and internal organization of nucleoli (3,15,16,18). Phase separation mechanisms have also been suggested to drive heterochromatin formation via HP1 during fly development (54). Treatment of fly S2 or mouse NIH3T3 cells with 1,6-hexanediol (1,6-HD), an aliphatic alcohol disrupting weak hydrophobic interactions, resulted in partial dispersal of HP1 proteins from heterochromatin domains (54). To assess the impact of disrupting weak hydrophobic interactions on the formation of and interactions between chromocenters and nucleoli as a function of HP1 protein levels, we treated control and mutant ESCs with 1,6-HD.

Treatment of control JM8 ESCs for 2.5 min with 0.5% or 2% 1,6-HD prior to fixation resulted in a major reduction of the overall volume of nuclei as well as its nucleoli and chromocenters (Supplementary Figures S5A–S5C), as reported previously (54). IF staining for NPM1 and FBL revealed a partial dispersal of these proteins from nucleoli into the nucleoplasm and onto chromocenters. Staining of genomic DNA showed reduced DAPI signals at chromocenters and increased intensities at nucleoli, possibly pointing to mixing of both compartments (Figure 4A, 4B). These data underscore the importance of weak hydrophobic interactions in structuring and compartmentalizing nuclei of ESCs.

We then investigated the impact of 1,6-HD treatment on nucleolar formation during the cell cycle. Treatment of control ESCs with 2% 1,6-HD for 5 min caused a significant decrease in nucleolar solidity in S and G2 but not in G1 populations, thereby closely phenocopying the nucleolar impairment observed in *Hp1α/β*-DKO ESCs (Figure 4C). Interestingly, HP1β intensities at PCH were partially decreased upon 1,6-HD treatment (Figure 4D). In contrast 1,6-HD treatment did not further reduce nucleolar solidity levels in cells lacking HP1α/β proteins (Figure 4E).

Given these results, we examined whether 1,6-HD treatment causes mixing of nucleoli with chromocenters only or with euchromatic compartments as well by quantifying H3K9me3 and H3K4me3 levels within nucleoli. Whereas both marks were elevated at nucleoli in control ESCs upon 1,6-HD treatment, only H3K9me3 was elevated in *Hp1α/β*-deficient ESCs, irrespectively of 1,6-HD treatment (Figure 4F, 4G). Thus, these experiments show that HP1α/β depletion restricts the dynamic responses of different nuclear compartments to perturbations of weak hydrophobic interactions by 1,6-HD exposure. We further conclude that HP1 sequesters chromocenters away from nucleoli thereby preserving overall nuclear organization.

Major satellites transcripts accumulate in nucleoli of HP1 deficient ESCs

We next investigated possible mechanisms underlying nucleolar deformation in *Hp1α/β* deficient ESCs. Changes in nucleolar size and morphology have been linked to mis-regulation of genes involved in ribosome biogenesis, such as ribosomal subunits and rRNA processing factors (87–90), loss of pluripotency and differentiation of ESCs (25), or heat shock effects (3). We dismiss such possibilities since transcriptome analysis did not show deregulation of ribosome-related, pluripotency nor heat shock genes among the 105 significantly up- and 207 down-regulated genes in *Hp1α/β-DKO* ESCs (Figure 5A, Supplementary Figure S6A–S6C, Tables S1 and S2).

We further discount a direct role of HP1 proteins in nucleolar function in naive ESCs since previous immunoprecipitation coupled to mass spectrometry detection studies failed to detect interactions between structural components of nucleoli and HP1 proteins in such cells (67,91,92). Likewise, we neither observed HP1α/β enrichments at nucleoli in control ESCs (Supplementary Figures S1B, S1C). We performed ChIP-qPCR experiments to measure H3K9me3 levels at promoter sequences of rDNA repeat loci. We observed about 2-fold reduced levels in *Hp1α/β*-DKO ESCs (Figure 5B, 5C), negating the idea of abnormal heterochromatinization of rDNA sequences and cellular differentiation in absence of HP1α/β proteins.

We next investigated in which way degenerated pericentromeric heterochromatin underlying chromocenters (Supplementary Figure S1) may impair nucleolar integrity. Importantly, ChIP-qPCR revealed a decrease in H3K9me3 occupancy at major satellite sequences (Figure 5B, 5C), which may facilitate aberrant transcription as observed in *Suv39h1/2* deficient ESCs (82,93). To measure major satellite expression, we performed strand specific RNA-FISH analysis (Figure 5D-G). Forward and reverse strands were predominantly expressed during S phase in control and mutant cells, which is consistent with reported replication dependency of major satellite transcription (94). Additionally, we detected significant de-repression of major satellites at chromocenters throughout the entire cell cycle in *Hp1α/β*-DKO ESCs (Figure 5D–5G), in line with reduced H3K9me3 levels (Figure 5C, Supplementary Figure S1G). Forward and reverse RNA-FISH signals were more diffusely localized at and around PCH foci and, importantly, levels were significantly elevated within nucleoli of *Hp1α/β*-DKO ESCs (Figure 5D, 5F).

To assess whether such satellite transcripts directly interact with nucleolar components we performed RNA immunoprecipitation (RIP) for GFP-NPM1 on transiently transfected control and *Hp1α/β*-DKO ESCs, followed by RT-qPCR (Figure 5H, I). As expected, *18S* rRNA was efficiently recovered in the GFP-NPM1 pulldown, both in control and mutant populations. The recovery of major satellite RNA with GFP-NPM1 was dramatically increased in the absence of HP1α/β whereas we did not observe enrichments for *b-actin* mRNA nor for *Line1* ncRNA (data not shown).

These data indicate that pericentromeric major satellites are aberrantly transcribed throughout the cell cycle in absence of HP1α/β proteins. We propose that such satellite transcripts perturb the spatial separation between PCH regions and nucleoli from G1 phase onwards and thereby interfere with nucleoli formation during cell cycle progression.

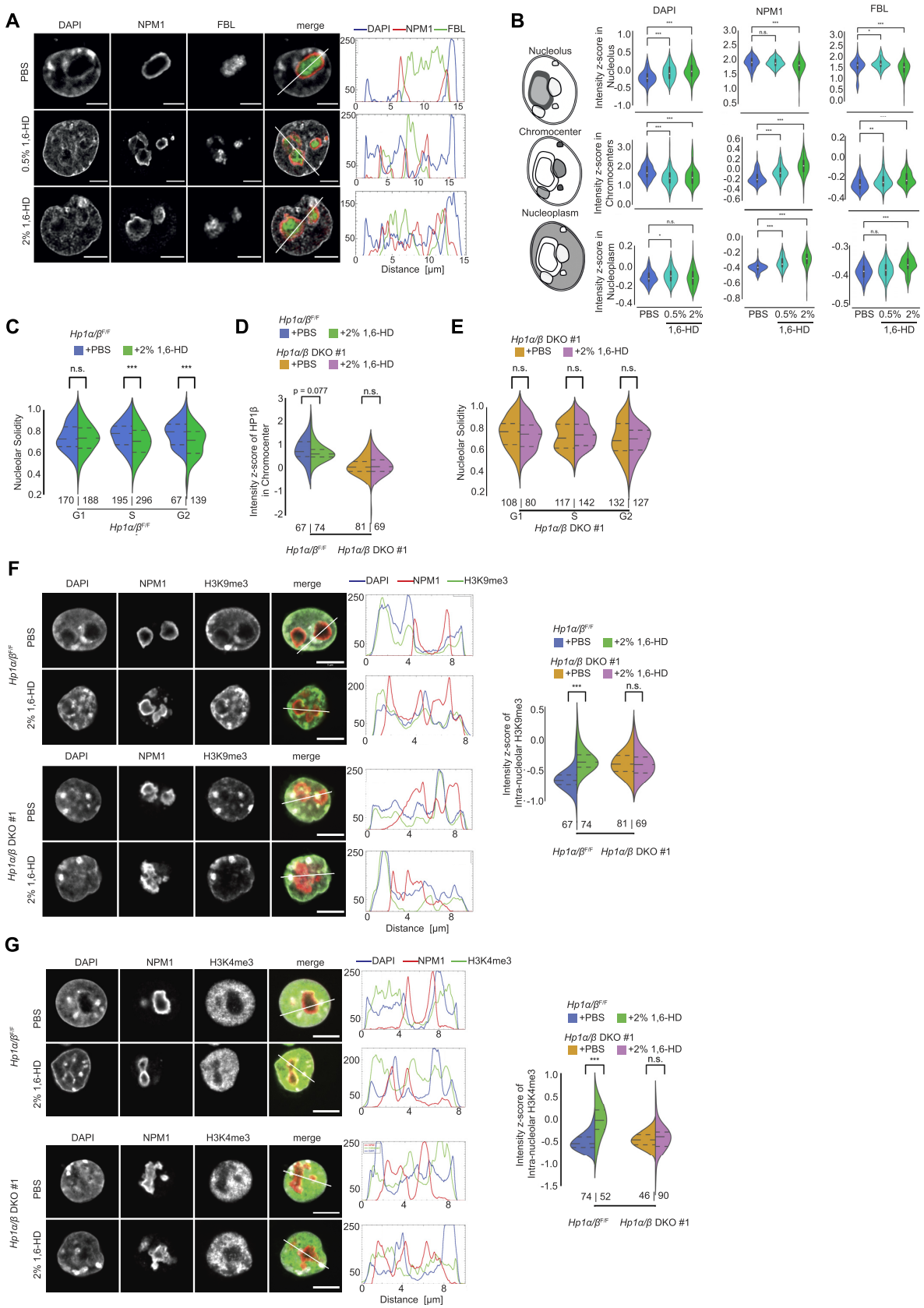

Figure 4. 1,6-Hexanediol treatment phenocopies the nucleolar defects seen upon *Hp1α/β* deficiency. (**A**) Left panels: Representative IF staining against NPM1 and FBL of control JM8 ESCs treated with PBS, 0.5% or 2% 1,6-hexanediol (in PBS) for 2.5 min prior to fixation. Central slices of confocal

HP1 dimerization ability and localization at PCH are required for nucleolus-PCH partitioning and preservation of nucleolar structural integrity

We next investigated whether exogenous HP1 expression can reinstate structural and functional integrity of nucleoli in *Hp1α/β*-DKO ESCs. We transiently transfected ESCs with Myc-tagged full-length Hp1α or Hp1β constructs. Both proteins were efficiently expressed and targeted to PCH, and were able to completely restore nucleolar structural defects in S phase (Figure 6A-6D, Supplementary Figure S7A) demonstrating functional redundancy between HP1α and HP1β in regulating nucleolar morphology.

To assess which HP1 domains were required for the preservation of nucleolar stability we transfected *Hp1α/β*-DKO ESCs with truncated or full-length HP1β point mutants that selectively abrogate (i) binding of the chromo domain (CD) to H3K9me2/3 (HP1β$^{\Delta CD}$, HP1β^{V23M}), (ii) dimerization of the chromo shadow domain (CSD) and/or interactions with PxVxL-motif containing partners (HP1β$^{\Delta CSD}$, HP1β^{L168H}, HP1β^{I161E}) or (iii) interaction of the CSD with PxVxL-containing proteins without affecting dimerization (HP1β^{W170A}) (35,36,45,46,76,95) (Figure 6A). The different complementation constructs were expressed at comparable levels (Supplementary Figure S7A). The two mutants with impaired capacity of binding H3K9me2/3 (HP1β$^{\Delta CD}$, HP1β^{V23M}) showed rather poor enrichment at PCH and increased nucleoplasmic localization (Figure 6B, 6E), as reported previously (41,56). PCH localization of the CSD deletion mutant HP1β$^{\Delta CSD}$, and of the two dimerization mutants HP1β^{I161E} and HP1β^{L168H} was detectable, but clearly reduced compared to wild-type HP1β (41) (Figure 6B). In contrast, HP1^{W170A}, which can undergo dimerization but lacks the ability to bind PxVxL-motif proteins, was largely unaffected in its localization to PCH foci (Figure 6B, 6E). These data indicate that binding of HP1β to PCH in ESCs requires both the CD as well as CSD-mediated dimerization of HP1β, as has been suggested previously for other cell types (36,41,42,49,95). Interactions with PxVxL-motif binding partners is, however, not required for PCH localization.

Both HP1β$^{\Delta CD}$ and HP1β$^{\Delta CSD}$ truncated proteins failed to rescue the nucleolar phenotype, demonstrating that both domains contribute to the regulation of nucleolus structure (Figure 6F). Importantly, the dimerization mutant HP1β^{I161E} was neither able to reinstate normal nucleolar morphology. We confirmed this result by expressing the HP1β^{L168H} mutant. The HP1β^{L168} residue in the CSD normally participates in forming the dimerization interface. It also interacts with PxVxL-proteins (46) (Figure 6F). Remarkably, transient transfection with HP1β^{W170A} completely rescued the nucleolus solidity defect seen in *Hp1α/β*-DKO ESCs (Figure 6F), indicating that the dimerization of HP1β, but not its binding to PxVxL-containing interactors, is required for preserving nucleolar structural integrity.

Unexpectedly, we also observed rescue of nucleolar solidity upon expression of HP1β^{V23M}, which has been shown to display impaired affinity for H3K9 methylation (35,36,96) (Figure 6F). Given that a small fraction of HP1^{V23M} is retained at PCH foci (Figure 6B, 6E), despite the impaired capacity of this mutant to bind H3K9me2/me3, we reasoned that moderate enrichment of HP1 at PCH in ESCs could be achieved through binding to PxVxL-motif containing proteins (81,84,97,98). To test this possibility, we transfected *Hp1α/β*-DKO ESCs with a double-mutated HP1β$^{V23M/W170A}$ protein (Figure 6A), which lacks both the ability to bind H3K9me2/3-marked chromatin as well as to interact with PxVxL-containing partners. Whereas HP1β^{WT}, HP1β^{W170A} and to a lesser extent HP1β^{V23M} showed significant enrichment at segmented PCH, HP1β$^{V23M/W170A}$ protein failed to enrich at PCH (Figure 6B, 6E), despite comparable expression levels (Supplementary Figure S7A).

We note that these findings agree with previous studies on HP1β localization (41) reporting reduced PCH occupancy of an alternate CD/CSD double mutant HP1β$^{W42L/W170A}$ compared to just HP1β^{W42L} alone. These data indicate that, while CD interactions with H3K9me2/me3 are undoubtedly important for proper localization of HP1β to PCH, additional interactions between the CSD and PxVxL-motif proteins contribute further to its stable binding and retention.

Significantly, we found that expression of HP1β$^{V23M/W170A}$ was the least efficient in rescuing the nucleolar structural defects of *Hp1α/β*-DKO ESCs (Figure 6F), arguing that the presence of HP1 at PCH is indeed crucial for maintaining intact nucleolar morphology. Altogether, these data indicate that the regulation of nucleolar integrity is connected to two key properties of HP1: (i) threshold enrichment of HP1α/β at PCH, which can be reached through redundant mechanisms such as binding to H3K9me3-marked chromatin and interactions with PxVxL-motif containing components present at constitutive heterochromatin and (ii) the ability of HP1 molecules

z-stacks are shown. Right panels: Line scans indicate (co)localization between DAPI (blue), NPM1 (red) and FBL (green) signals. All scale bars = 5 μm. (**B**) Violin plots showing the quantification of DAPI (left), NPM1(middle) and FBL (right) signal intensities inside nucleoli (upper), at PCH (middle) or in the nucleoplasm (lower) (normalized to total nuclear signal intensities, respectively) in control JM8 ESCs treated with PBS or 1,6-hexanediol as described in (A). (**C**) Violin plots showing the quantification of nucleolar solidity in G1, S and G2 of control (*Hp1α$^{F/F}$; Hp1β$^{F/F}$*) ESCs treated with PBS or 2% 1,6-hexanediol for 5 min prior to fixation. Based on IF staining against NPM1 and FBL. (**D**) Violin plots showing the z-score normalized intensities of HP1β at PCH in control (*Hp1α$^{F/F}$; Hp1β$^{F/F}$*) and *Hp1α/β*-DKO ESCs treated with PBS or 2% 1,6-hexanediol for 5 min prior to fixation. (**E**) Violin plots showing the quantification of nucleolar solidity in G1, S and G2 of *Hp1α/β*-DKO ESCs treated with PBS or 2% 1,6-hexanediol for 5 min prior to fixation. Based on IF staining against NPM1 and FBL. (**F, G**) Left panels: Representative IF staining against NPM1 and H3K9me3 (F) or H3K4me3 (G) of control (*Hp1α$^{F/F}$; Hp1β$^{F/F}$*) and *Hp1α/β*-DKO ESCs treated with PBS or 2% 1,6-hexanediol for 5 min prior to fixation. DNA was stained with DAPI. Central slices of confocal z-stacks are shown. Scale bars = 5 μm. Middle panels: Line scans indicate (co)localization between DAPI (blue), NPM1 (red) and H3K9me3 (F) or H3K4me3 (G) (green) signals. Right panel: Violin plots showing the quantification of intra-nucleolar H3K9me3 (F) or H3K4me3 (G) in control (*Hp1α$^{F/F}$; Hp1β$^{F/F}$*) and *Hp1α/β*-DKO ESCs upon treatment with PBS or 2% 1,6-hexanediol for 5 min prior to fixation. Sample sizes are indicated below each violin. * $P < 0.05$, ** $P \leq 0.01$, *** $P \leq 0.001$ (Mann–Whitney *U*-test).

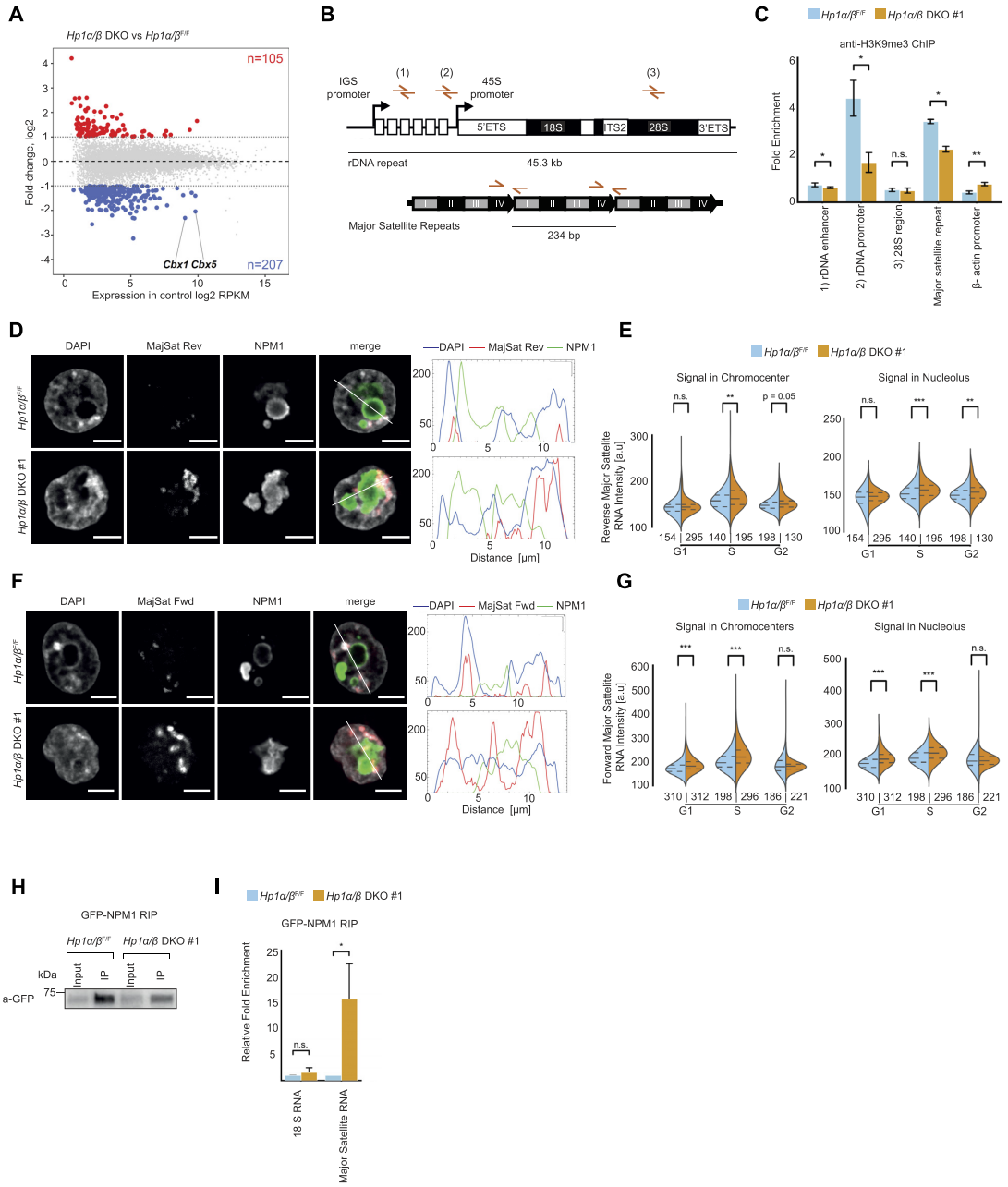

Figure 5. Major satellite transcripts accumulate in aberrant nucleoli in *Hp1α/β* deficient ESCs. (**A**) MA plot (B) representing differential gene expression analysis of *Hp1α/β*-DKO versus control ESCs. Numerical data is available in Supplementary Table S1. (**B**) Schematic representation of a mouse rDNA repeat (upper) and major satellite repeats (lower) with highlighted positions of the primers used for ChIP-qPCR. (**C**) Bar plot representing H3K9me3 ChIP-qPCR analysis of the fold enrichment (mean and standard deviation, $n = 3$) of designated rDNA loci depicted in the Figure 6D along with major satellite DNA as a positive control and beta-actin promoter as a negative control, isolated from a-H3K9me3 ChIP relative to an IgG ChIP control. * $P < 0.05$, ** $P \leq 0.01$, *** $P \leq 0.001$ (two-sided, unpaired *t*-test). (**D**) Representative RNA-FISH detecting reverse major satellite repeat transcripts coupled to IF staining against NPM1 in control ($Hp1\alpha^{F/F}$; $Hp1\beta^{F/F}$) and *Hp1α/β*-DKO ESCs. DNA was stained with DAPI. Central slices of confocal z-stacks are shown. Scale bars = 5 µm. Line scans indicate (co)localization between DAPI (blue), major satellite repeat RNA (red) and NPM1 (green) signals. (**E**) Violin plots showing the absolute levels of fluorescence intensity of reverse major satellite repeat RNA-FISH signal at chromocenters (left) and nucleolus (right) in control ($Hp1\alpha^{F/F}$; $Hp1\beta^{F/F}$) and *Hp1α/β*-DKO ESCs (from D). (**F**) Representative RNA-FISH detecting forward major satellite repeat transcripts coupled to IF staining against NPM1 in control ($Hp1\alpha^{F/F}$; $Hp1\beta^{F/F}$) and *Hp1α/β*-DKO ESCs. DNA was stained with DAPI. Central slices of confocal z-stacks are shown. Scale bars = 5 µm. Line scans indicate (co)localization between DAPI (blue), major satellite repeat RNA (red) and NPM1 (green) signals. (**G**) Violin plots showing the absolute levels of fluorescence intensity of forward major satellite repeat RNA-FISH signal at chromocenters (left) and nucleolus (right) in control ($Hp1\alpha^{F/F}$; $Hp1\beta^{F/F}$) and *Hp1α/β*-DKO ESCs (from F). Sample sizes for (E) and (G) are indicated below each violin. * $P < 0.05$, ** $P \leq 0.01$, *** $P \leq 0.001$ (Mann–Whitney *U*-test). (**H**) Immunoblots for GFP-NPM1 input and immunoprecipitated fractions from transiently transfected control ($Hp1\alpha^{F/F}$; $Hp1\beta^{F/F}$) and *Hp1α/β*-DKO ESCs. (**I**) Bars plots representing RT-qPCR analysis of the fold enrichment (mean and standard deviation, $n = 3$ (three RNA extractions from two independent transfections for each biological sample)) of 18S rRNA and major satellite RNA isolated by anti-GFP-NPM1 RIP relative the control RIP after normalization to the respective input. GFP-NPM1 or control GFP were transfected into control ($Hp1\alpha^{F/F}$; $Hp1\beta^{F/F}$) and *Hp1α/β*-DKO ESCs. * $P < 0.05$, ** $P \leq 0.01$, *** $P \leq 0.001$ (two-sided, unpaired *t*-test).

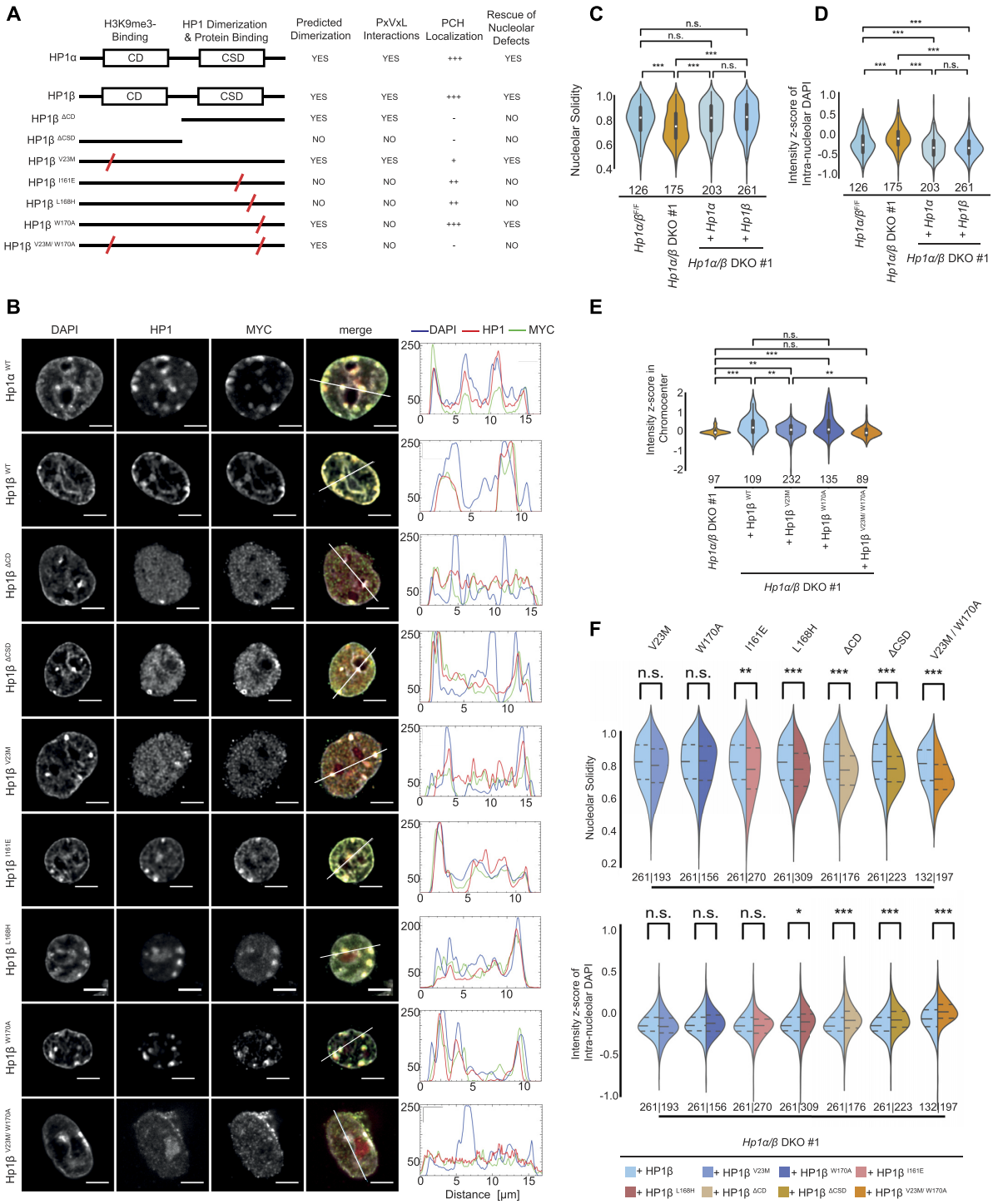

Figure 6. Restoring nucleolar defects in *Hp1α/β* deficient ESCs. (**A**) Schematic representation of truncated or point mutated HP1α and HP1β constructs. All constructs carry an N-terminal 3xMyc-tag. Synopsis of the features of the constructs in terms of predicted dimerization, PxVxL interaction, PCH localization, and rescue of nucleolar defects. (**B**) Left panels: Representative IF staining against HP1β and Myc for detection of subnuclear localization of HP1β constructs shown in (A) transfected into *Hp1α/β*-DKO ESCs. Central slices of confocal z-stacks are shown. Scale bars, 5 µm. Right panels: Line scans indicate (co)localization between chromocenters (DAPI- bright, blue) and HP1β construct (anti-HP1β in red; anti-Myc in green). Note that different anti-HP1β antibodies were used for detection of truncated constructs (see Materials & Methods). (**C, D**) Violin plots showing the quantification of nucleolar solidity (C) and intra-nucleolar DAPI (D) in control ($Hp1\alpha^{F/F}$; $Hp1\beta^{F/F}$) and *Hp1α/β*-DKO ESCs (in S phase) upon transient transfection with full-length $HP1\alpha^{WT}$ or $HP1\beta^{WT}$. Based on IF staining against NPM1 and FBL. (**E**) Violin plots showing the quantification of *z*-score normalized intensities of indicated HP1β point mutants transfected into *Hp1α/β*-DKO ESCs from (B) at PCH. (**F**) Violin plots showing the quantification of nucleolar solidity (upper panel) and intra-nucleolar DAPI (lower panel) in *Hp1α/β*-DKO ESCs (in S phase) upon transient transfection with indicated truncated or point mutated HP1β constructs. Based on IF staining against NPM1, FBL and DAPI. Sample sizes are indicated below each violin. * $P < 0.05$, ** $P \leq 0.01$, *** $P \leq 0.001$ (Mann–Whitney *U*-test).

to dimerize and/or oligomerize once sufficiently recruited to PCH.

Nucleolar defects are phenocopied in *Suv39h* dn ESCs

To further investigate the dependency of nucleolar integrity on PCH composition we turned our attention to ESCs deficient for the SUV39H1/H2 or SUV4-20H1/H2 HMTases, acting up- and downstream of HP1 in depositing pericentromeric H3K9me3 and H4K20me3, respectively (34,36,83).

Suv39h dn ESCs lacked enrichment of H3K9me3 and HP1α/β/γ paralogs at PCH (Supplementary Figure S8A) (82). *Suv39h* dn ESCs also displayed reduced nucleoli numbers and nuclear sizes, as observed in *Hp1α/β*-DKO ESCs, suggesting an altered nuclear configuration. Chromocenter numbers and volumes as well as nucleolar volumes were, however, only slightly more variable in mutant than control cells (Supplementary Figures S8B-S8F). As shown previously (93), we detected derepression of major satellites in *Suv39h* dn ESCs, with RNA-FISH signals elevated both at chromocenters and within nucleoli (Figure 7A, 7B). Notably, we observed structural defects in nucleoli of *Suv39h* dn ESCs in S phase, which were highly reminiscent of those observed in *Hp1α/β*-DKO ESCs (Figure 7C). Accordingly, nucleolar solidity was significantly reduced in both *Suv39h* dn ESC clones analyzed (Figure 7C, 7D).

Suv4-20h dn ESCs lack H4K20me3 but retain H3K9me3 and HP1*β* at PCH (Supplementary Figures S8G, S8H) (83,99). Contrary to *Suv39h* dn and HP1α/β DKO ESCs, *Suv4-20h* dn ESCs exhibited slightly larger nuclei, chromocenter volumes and increased number of chromocenters (Supplementary Figures S8I–S8K), pointing to more relaxed heterochromatin, as reported for *Suv4-20h* dn MEFs (43). Further, levels of major satellite repeat RNAs were not elevated in *Suv4-20h* dn ESCs and, importantly, nucleolar morphology was not perturbed (Figure 7E–7H, Supplementary Figure S8L, S8M). Hence, *Suv4-20h*-controlled processes such as cohesin recruitment at PCH are not required to safeguard nucleolar integrity (43).

Besides their well-established role in the *Suv39h* pathway at constitutive heterochromatin, HP1 proteins also form stable complexes with the zinc finger transcription factor ADNP1 and the chromatin remodeler CHD4 (67). In mouse ESCs, this complex, termed ChAHP, represses endodermal gene transcription in a H3K9me3-independent manner. ChAHP further modulates 3D nuclear organization and chromatin looping in ESCs by competing with CTCF for binding to SINE elements dispersed throughout the mouse genome (100). Even so, we did not detect alterations to nucleolar structure in *Adnp1* KO ESCs (Supplementary Figure S8N, S8O), negating the possibility that the nucleolar defects observed in *Hp1β* single and *Hp1α/β* DKO ESCs are due to lack of HP1β function in the ChAHP complex.

Together, our findings strongly imply an association between the chromatin configuration at PCH, notably enrichment of H3K9me3 and HP1 proteins, and the structural integrity of nucleoli. Although we cannot exclude the possibility that the SUV39H-HP1 pathway functions in ESCs at other genomic regions to preserve nucleolar structure and function, we deem it unlikely since SUV39h-dependent H3K9me3 enrichments are found almost exclusively at pericentromeric and intergenic major satellite repeats apart from some ERV and LINE elements (101). We favour a model in which SUV39H1/2-mediated H3K9me3 and recruitment of HP1 proteins modulate biophysical properties of chromocenters to confer functional sovereignty to PCH and nucleoli, for instance by restricting major satellite repeat transcription and/or preventing such transcripts from 'escaping' into neighbouring nuclear domains.

Nucleolar defects are accompanied by reduced rRNA synthesis

To investigate the impact of altered pericentromeric and nucleolar structures and nuclear localizations on cellular physiology, we performed proliferation assays. During the initial derivation and expansion of both *Hp1β*-KO and *Hp1α/β*-DKO ESC clones, we noticed a brief phase of impaired growth which lasted for approximately two weeks (Supplementary Figure S9A). The established single and double mutant ESC clones, however, recovered following continued passaging, both in terms of proliferation and colony morphology (Supplementary Figures S9B, S9C).

Remarkably, we observed a dramatic reduction in colony size and cell proliferation in *Hp1α/β*-cDKO cells after two days of 4-OHT treatment (Figure 8A–8C), resembling the defects observed during the initial derivation of the constitutive mutant cell lines. *Hp1α/β*-cDKO ESCs didn't display abnormalities in their cell cycle profiles (Supplementary Figure S9D) and revealed only a modest increase of ∼4% in cell death (Supplementary Figure S9E). Hence, the reduction in cell proliferation more likely reflects a slow growth phenotype rather than resulting from impaired cell viability or cell cycle checkpoint activation. Slow growth phenotypes have been reported for several congenital or somatic tissue-specific ribosomopathy diseases which are caused by mutations in ribosomal proteins or ribosome biogenesis factors. Such mutations affect the processing of ribosomal RNAs (rRNAs) and ribonucleoproteins, disrupting the integrity of nucleoli and leading to a shortage of mature ribosomes and generally hypo-proliferation (15,102,103).

To measure the impact of *Hp1α/β* deficiency on rRNA synthesis, we quantified rRNA levels throughout the rDNA locus. Constitutive and conditional deletion of HP1α/β resulted in significantly reduced levels of the mature 28S rRNA transcript. rRNA levels in single *Hp1β*-KO cells was unaffected (Figure 8D, 8E).

We next profiled levels of immature pre-processed 45S pre-rRNA transcripts using primer sets located within the 5′ external transcribed spacer (5′ ETS) and internal transcribed spacer 2 (ITS2) regions, as well as within the upstream intergenic spacer transcript (IGS). We measured approximately two-fold reductions in *Hp1α/β*-cDKO ESCs (Figure 8D, 8F). These data argue that the decreased level of mature rRNAs is linked to impaired rRNA synthesis. In addition, the ratio between 28S and 18S rRNAs was slightly reduced between *Hp1α/β*-DKO and control ESCs (Figure 8G) suggesting compromised pre-rRNA processing.

Given the appearance of the structural nucleolar defects in *Hp1α/β* deficient ESCs in S phase, we investigated cell

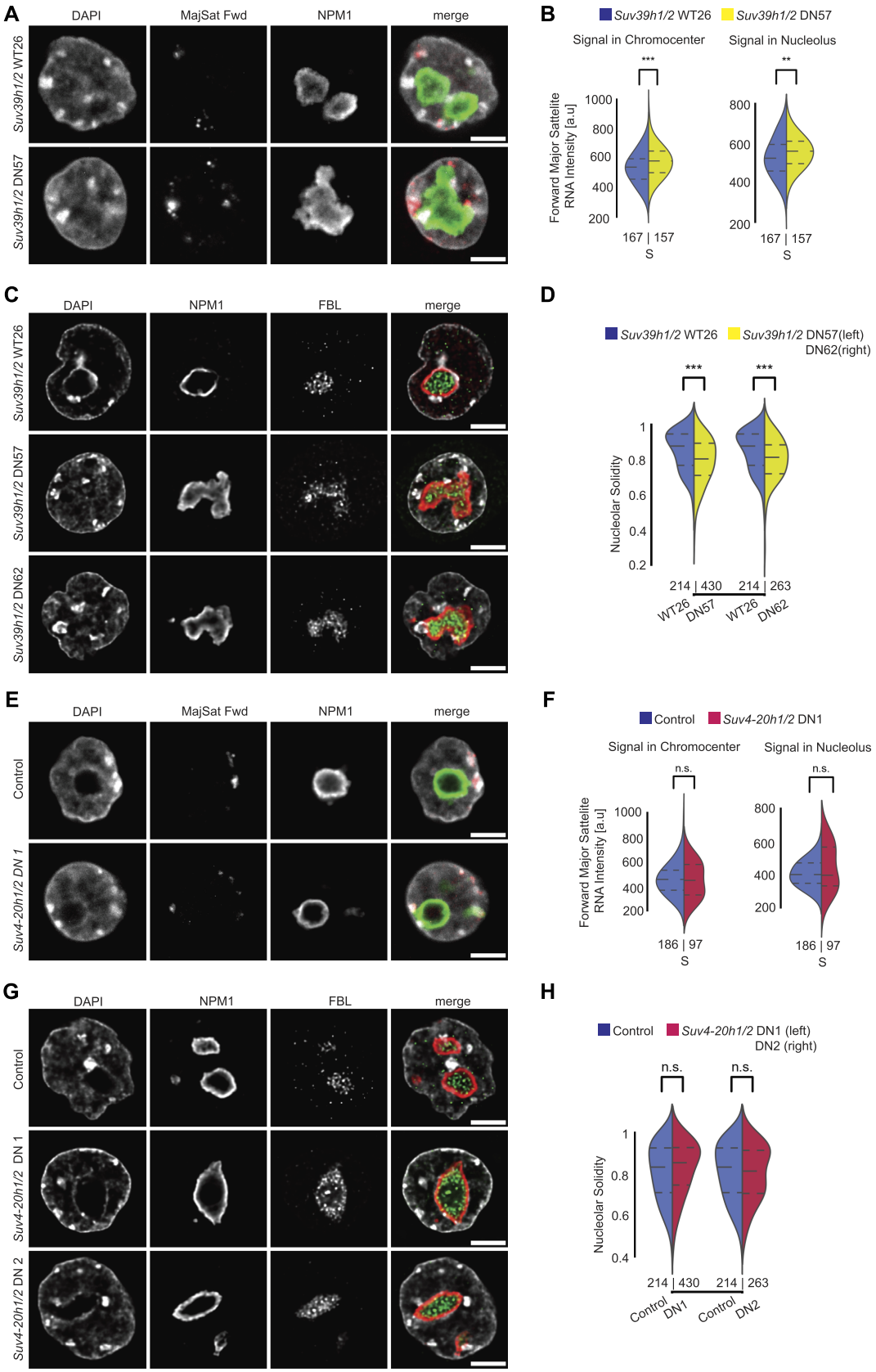

Figure 7. Nucleoli morphology in control, *Suv39h1/2* double null and *Suv4-20h1/2* double null ESCs. (**A**) Representative RNA-FISH detecting forward major satellite repeat transcripts coupled to IF staining against NPM1 in control and *Suv39h1/2* dn ESCs in S phase. DNA was stained with DAPI.

cycle dependence of rDNA transcription. rRNA synthesis is known to be lowest in G1 and to increase in S phase due to the cell cycle-dependent regulation of the Pol I transcription factor UBF (104). Indeed, 28S rRNA levels peaked in S phase in control ESCs (Figure 8G–I). In contrast, they remained fairly stable throughout the cell cycle in both *Hp1α/β*-cDKO and *Hp1α/β*-DKO ESCs as assessed by RT-qPCR (Figure 8H, 8I) and RNA electrophoresis (Figure 8G).

Cell cycle-phase normalized analysis revealed a ∼2-fold decrease in 28S rRNA levels during S phase in *Hp1α/β*-cDKO relative to control ESCs whereas rRNA levels in G1 and G2 were comparable between genotypes (Figure 8J). In constitutive *Hp1α/β*-DKO ESCs at late passage (>20), however, 28S levels were elevated in G1 and G2 phase compared to control cells (Figure 8K), suggesting that these cells may have potentially compensated for the impaired rRNA synthesis in S phase by increasing baseline rRNA transcription. Adaptation of transcriptional outputs provides an attractive mechanism to explain the discrepancies in cell proliferation between early passage/conditional and later passage HP1 mutants (Figure 8A, 8B, 8C, Supplementary Figure S9A, S9C).

Finally, we transiently expressed HP1β^{WT}, HP1β^{V23M}, HP1β^{W170A} and HP1β$^{V23M/W170A}$ proteins in *Hp1α/β*-DKO ESCs. Expression of control and single residue mutant proteins, but not of the double residue mutant HP1β protein resulted in moderately increased 28S rRNA levels, reaffirming a link between restoring nucleolar morphology and elevating rRNA synthesis (Figures 6A and 8L).

DISCUSSION

A role for heterochromatin in regulating nucleolar stability

Here we reveal an essential role for HP1β and HP1α in safeguarding the structural integrity and function of nucleoli. *Hp1α/β*-deficiency perturbs the internal tripartite organization of nucleoli and alters their morphology from dynamic round shapes into more static amorphous appearances during the progression of the cell cycle. Comparable morphological alterations have been reported to occur upon prolonged heat shock exposure causing irreversible changes in protein composition of nucleoli (3). Likewise, reduced levels of particularly late-assembling ribosomal proteins of 60S subunits majorly affect nucleolar structure and function (7,89).

Contrary to ribosomal proteins, HP1 proteins have not been detected in nucleoli of undifferentiated ESCs (Supplementary Figures S1B, S1C, S1D) (67,91,92), suggesting an indirect role for these heterochromatic proteins in modulating nucleolar integrity. Indeed, the appearance of nucleolar deformations in mid-late interphase in *Hp1α/β*-deficient ESCs coincided spatially with increased proximity of chromocenters to aberrant nucleoli, at times resulting even in partial engulfment of chromocenters by nucleoli. Absence of HP1α/β proteins and reduced H3K9me3 and HP1γ levels at chromocenters resulted in increased quantities of forward and reverse transcripts of major satellites. These transcripts accumulated within associated nucleoli which likely underlies their increased level of interactions with NPM1 proteins.

De-repressed major satellites along with nucleolar defects in S phase were also observed in *Suv39h* dn but not *Suv4-20h* dn ESCs, indicating that enrichment of H3K9me3 and HP1 proteins rather than H4K20me3 and possibly cohesin at PCH (43) are instructive for preserving nucleolar structure. In agreement with this notion, the severity of nucleolar deformation scaled to some extent with levels of pericentromeric H3K9me3 and major satellite transcripts across our different mutant cell lines. E.g. nucleolar morphology was only moderately impaired in nuclei of the *Hp1α/β*-DKO #2 ESC line, which exhibited even slighty increased H3K9me3 levels and low levels of major satellite transcripts (data not shown), contrasting the prominent phenotypes observed in *Hp1α/β*-DKO #1, *Hp1α/β*-cDKO and both *Suv39h* dn ESC lines. Typically, loss of HP1 proteins is followed by a decrease in pericentromeric H3K9me3 due to partial co-dependency of HP1 and SUV39H1/2 in their recruitment to PCH and impaired protein stability of unbound SUV39H1/2 (96,99). It is conceivable that adaptive responses (such as increased SUV39H1/2 activity or compensation by other HMTases like SETDB1) during the initial derivation of *Hp1α/β*-DKO #2 may have resulted in retention of high H3K9me3 levels at PCH following HP1α/β removal, thereby mitigating adverse effects on chromocenter and nucleolar structural integrity.

Intriguingly, the mobility of NPM1 within the GC was reduced, highlighting biophysical alterations within nucleoli of *Hp1α/β* deficient ESCs. We propose that accumulation of aberrant exogenous transcripts like major satellites in nucleoli disturbs the homeostatic LLPS interactions between various rRNA transcripts and nucleolar RNA-binding factors such as NPM1 and FBL, ultimately affecting the internal nucleolar structural compartmentalization and efficiency of rRNA biogenesis. Consistently, we could partially phenocopy the nucleolar integrity defects by exposing control ESCs with 1,6-hexanediol, an aliphatic alcohol that was

←

Central slices of confocal z-stacks are shown. Scale bars = 5 μm. (**B**) Violin plots showing the absolute levels of fluorescence intensity of forward major satellite repeat RNA-FISH signal at chromocenters (left) and nucleolus (right) in control and *Suv39h1/2* dn ESCs (from A). (**C**) Representative IF staining against NPM1 and FBL in S phase of control and two *Suv39h1/2* dn ESCs. DNA was stained with DAPI. Central slices of confocal z-stacks are shown. Scale bars = 5 μm. (**D**) Violin plots showing the quantification of nucleolar solidity in S phase of control and two *Suv39h1/2* dn ESCs from (C). (**E**) Representative RNA-FISH detecting forward major satellite repeat transcripts coupled to IF staining against NPM1 in control and *Suv4-20h1/2* dn ESCs in S phase. DNA was stained with DAPI. Central slices of confocal z-stacks are shown. Scale bars = 5 μm. (**F**) Violin plots showing the the absolute levels of fluorescence intensity of forward major satellite repeat RNA-FISH signal at chromocenters (left) and nucleolus (right) in control and *Suv4-20h1/2* dn ESCs (from E). (**G**) Representative IF staining against NPM1 and FBL in S phase of control and two *Suv4-20h1/2* dn ESCs. DNA was stained with DAPI. Central slices of confocal z-stacks are shown. Scale bars = 5 μm. (**H**) Violin plots showing the quantification of nucleolar solidity in S phase of control and two *Suv4-20h1/2* dn ESCs from (G). Sample sizes for B, D, F, G are indicated below each violin. * $P < 0.05$, ** $P \leq 0.01$, *** $P \leq 0.001$ (Mann–Whitney *U*-test).

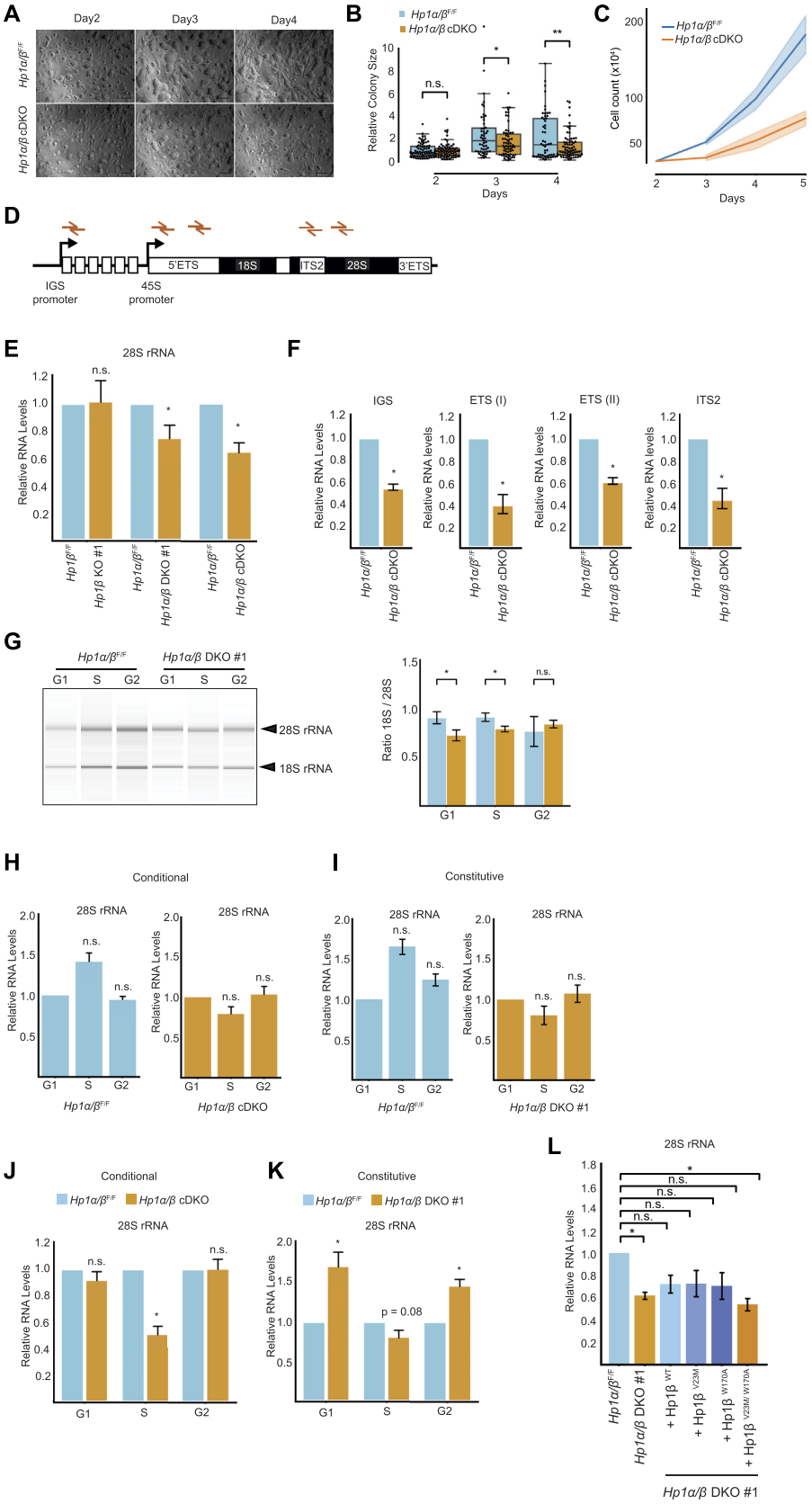

Figure 8. Cellular proliferation and rRNA expression are reduced in *Hp1α/β* deficient ESCs. (**A**) Brightfield microscopy images of $Hp1\alpha^{F/F}$; $Hp1\beta^{F/F}$; Cre-ERT2 ESCs colonies upon treatment with 1μM 4-OHT or EtOH for the indicated time periods. Scale bars = 100 μm. (**B**) Bar plots showing the

previously shown to cause partial dispersal of HP1 from PCH by perturbing weak hydrophobic interactions (54).

Previously, the SUV39H1/2 HMTases have been shown to prevent the occurrence of illegitimate interactions between individual PCH domains at the nuclear periphery during the onset of meiotic prophase of mouse male germ cells. This function ensures proper chromosome pairing, synapsis, progression through meiotic prophase and male fertility (34). Hence, the SUV39H1/2 and HP1 proteins appear to function as key regulators of heterochromatic integrity and providing functional sovereignty to constitutive heterochromatic chromocenters in different nuclear settings. Disorganization of nucleoli has also been reported in *Drosophila* salivary gland cells deficient for *Su(var)3–9* or *HP1*, which was attributed to reductions in H3K9me2 at repeat DNA (105), suggesting that generally the role of heterochromatin in regulating nuclear compartmentalization is evolutionarily conserved.

Nonetheless, beyond the proposed direct role at chromocenters, we cannot exclude the possibility that HP1α/β proteins function at other genomic regions to safeguard nucleolar integrity. For example, HP1α was recently identified to function in human U2OS cells as a chromatin crosslinker, providing mechanical strength to mitotic chromosomes and the nucleus throughout the cell cycle. Transient degradation of HP1α or expression of the HP1α^{I165E} dimerization mutant reduced short-extension nuclear stiffness and lowered solidity of nuclei, yet without releasing heterochromatin from the nuclear periphery nor changing overall levels of H3K9me2/3 (106,107).

Functional redundancy between HP1α and HP1β

As assessed by IF, transient expression of either HP1α or HP1β in *Hp1α/β*-DKO ESCs completely restored nucleolar solidity and reduced aberrant associations of nucleoli with DAPI-bright heterochromatin, indicating that both paralogs function redundantly in preserving the integrity of nucleolar and heterochromatic compartments in ESCs. Unique and redundant functions for HP1 paralogs in maintaining proper PCH configuration have previously been reported (77,81,96). Our western blot and immunofluorescence analysis revealed, however, unaltered cellular levels and residual HP1γ localization at PCH in HP1α/β DKO ESCs. It is therefore unlikely that HP1γ contributes to nucleolar stability in ESCs. Instead, Hp1γ and the H3K9me2 HMT G9a have even been reported to localize at actively transcribed rDNA loci in somatic cell lines. G9a was shown to facilitate pre-rRNA synthesis, to suppress R-loop formation at rDNA loci and to prevent fragmentation of nucleoli, a phenotype different from the irregular amorphously shaped nucleoli observed in *Hp1α/β*-DKO ESCs (108,109).

Despite a decrease in nucleolar solidity measured at the ultrastructural level, IF analysis and RT-qPCR experiments failed to detect major alterations to nucleolar structure and rRNA synthesis, respectively, in *Hp1β*-KO ESCs, implying an overall weaker nucleolar phenotype in these mutants compared to *Hp1α/β*-(c)DKO ESCs. Of note, *Hp1β*-KO ESCs also exhibited significantly decreased levels of HP1α at PCH. Thus, even low levels of HP1α or HP1β at PCH appear to be sufficient for ensuring normal morphology of nucleoli (at least at the resolution observed by light microscopy). In line with this, nucleolar integrity was largely reinstated in *Hp1α/β*-DKO ESCs by expression of the H3K9me2/me3 binding mutant HP1β^{V23M} (35,36,96), which showed only modest PCH occupancy. In contrast, HP1β truncations and full-length point mutants which abrogated chromocenter localization entirely (HP1β$^{\Delta CD}$, HP1β$^{\Delta CSD}$, HP1β$^{V23M/W170A}$) and/or were deficient for dimerization (HP1β$^{\Delta CSD}$, HP1β^{I161E}, HP1β^{L168H}) failed to do so. The inability of dimerization-defective HP1β mutants to rescue is not unexpected, given that dimerization of HP1 molecules has been implicated in most if not all heterochromatin-related HP1 functions, including H3K9me3 binding (36,42), recruitment of heterochromatin factors (43,44) and mediating biophysical properties of chromocenters (47,52–56).

Cell cycle dynamics and physiological consequences of nucleolar disruption

Intriguingly, the defects in nucleolar structure and PCH-nucleolus associations in *Hp1α/β-(c)DKO* ESCs were mostly observed in S and G2 phases of the cell cycle. These temporal dynamics could potentially reflect a situation whereby absence of HP1α/β is initially 'tolerated', allowing nucleoli to form normally in G1 but causing progressive accumulation of deformed nucleoli as nucleoli continue to undergo coalescence and further maturation during in-

←

quantification of *Hp1α/β*-cDKO ESC colony sizes (relative to Day 2). (**C**) Cell counts of *Hp1α$^{F/F}$; Hp1β$^{F/F}$*; Cre-ERT2 ESCs upon treatment with 1 μM 4-OHT or EtOH for the indicated time periods. Data are presented as the mean ± SEM ($n = 3$). (**D**) Schematic representation of a mouse rDNA repeat with highlighted positions of the primers used for RT-qPCR. (**E**) Bar plots showing the quantification of RT-qPCR for 28S rRNA in *Hp1β*-KO, *Hp1α/β*-DKO (at passage 15) and *Hp1α/β*-cDKO (after 4 days of 4-OHT treatment) compared to their corresponding controls ($n = 3$). Data were normalized to *b-actin* mRNA. (**F**) Bar plots showing the quantification of RT-qPCR for 5′ ETS, ITS2 and IGS rRNA in *Hp1α/β*-cDKO ESCs (after 4 days of 4-OHT treatment) compared to control (mock treated with EtOH) ($n = 3$). Data were normalized to *b-actin* mRNA. (**G**) Bar plots (right) showing the ratio from the quantification of band intensities for 18S and 28S rRNA in G1, S and G2 of control and *Hp1α/β*-DKO ESCs obtained by automated RNA electrophoresis (left) with Agilent 2100 Bioanalyzer ($n = 3$). Data were normalized to total RNA area. (**H**) Quantification of RT-qPCR for 28S rRNA in G1, S and G2 of control and *Hp1α/β*-cDKO ESCs (*Hp1α$^{F/F}$; Hp1β$^{F/F}$*; Cre-ERT2 ESCs after 4 days of mock EtOH or 4-OHT treatment, respectively) ($n = 3$). Data were normalized to *b-actin* mRNA and were compared to G1 for each genotype. (**I**) Quantification of RT-qPCR for 28S rRNA in G1, S and G2 of control (*Hp1α$^{F/F}$; Hp1β$^{F/F}$*) and *Hp1α/β*-DKO ESCs ($n = 3$). Data were normalized to *b-actin* mRNA and were compared to G1 for each genotype. (**J**) Quantification of RT-qPCR for 28S rRNA in G1, S and G2 of control and *Hp1α/β*-cDKO ESCs (*Hp1α$^{F/F}$; Hp1β$^{F/F}$*; Cre-ERT2 ESCs after 4 days of mock EtOH or 4-OHT treatment, respectively) ($n = 3$). Data were normalized to *b-actin* mRNA and were compared to control 28S levels at the corresponding cell cycle phase. (**K**) Quantification of RT-qPCR for 28S rRNA in G1, S and G2 of control *(Hp1α$^{F/F}$; Hp1β$^{F/F}$)* and constitutive *Hp1α/β*-DKO ESCs (passage > 20) ($n = 3$). Data were normalized to *b-actin* mRNA and were compared to control 28S levels at the corresponding cell cycle phase. (**L**) Quantification of RT-qPCR for 28S rRNA in *Hp1α/β*-DKO ESCs (at passage 15) transfected with indicated HP1β point mutants (n = 3). Data were normalized to *b-actin* mRNA. * $P < 0.05$, ** $P \leq 0.01$, *** $P \leq 0.001$ (two-sided, unpaired *t*-test).

terphase. The appearance of aberrantly formed nucleoli also concurs with increased levels of major satellite transcripts in chromocenters and within nucleoli at S phase, supporting the notion of major satellite accumulation in nucleoli as a factor contributing to nucleolar impairment. Importantly, cell cycle profiling of EdU labeled cell populations by flow cytometry were not suggestive of any defects in DNA replication which could elicit checkpoint activation. Hence, the reduction in cell proliferation more likely reflects a hypo-proliferative condition, rather than stemming from a defect in cell cycle regulation.

Cellular growth and proliferation are crucially dependent on an adequate supply of ribosomes to maintain protein synthesis levels. A critical aspect of cellular physiology thus falls on the appropriate regulation of rRNA biogenesis by means of the nucleolus. Accordingly, highly proliferative cells, such as ESCs or tumor cells, contain large nucleoli, indicative of high ribosome biosynthesis activity (25,110–112), whereas downregulation of rRNA synthesis is correlated with a reduction in nucleolar size (113). Moreover, the size of the nucleoli has been shown to correlate positively with nuclear size (114,115). Consistent with this notion, we observed a significant decrease in both nuclear and nucleolar volume upon deletion of HP1α/β, which was accompanied by a reduction in rRNA levels and cell proliferative capacity. Interestingly, *Hp1α/β*-DKO ESCs regained their proliferative potential following continued passaging, possibly in part through upregulation of baseline rRNA transcription. Similarly, a recent report (96) described severe growth defects upon conditional deletion of all three HP1 paralogs in mouse ESCs, whereas constitutive single or double HP1 mutants were viable.

We note that the *Hp1α/β* deficiency-induced nucleolar defects reported here are reminiscent of those defining human ribosomopathies. Historically, ribosomopathy disorders have been described as diseases caused by defects in ribosomal proteins, rRNA processing or ribosome assembly factors (19,116). These abnormalities manifest clinically in a diverse, tissue-specific manner but are typically characterized by hypo-proliferation at the cellular level.

In addition to 'classical' ribosomopathies, decreased nucleolar activity has also been linked to premature aging disorders such as Werner syndrome (117,118) and Cockayne syndrome (119), as well as neurodegenerative diseases such as Alzheimer's disease (120). Intriguingly, both Werner syndrome and Cockayne syndrome have been found to be associated with impairments in constitutive heterochromatin organization, including dramatic reduction of H3K9me3 and HP1 proteins (121,122). Relaxation of heterochromatin and de-repression of satellite DNA in the context of cellular senescence and during natural aging are well documented (123–126). Thus, decreased nucleolar function associated with heterochromatin loss may be common hallmarks of cell aging. Here, we provide evidence that HP1 proteins impact nuclear architecture and cellular physiology through PCH-dependent regulation of nucleolar structural integrity. Hence, the role of HP1 proteins as ribosomopathy and/or cellular aging modulating factors warrants further investigations.

DATA AVAILABILITY

The RNA-Seq datasets produced in this study are available in the following database: Gene Expression Omnibus GSE201907.

SUPPLEMENTARY DATA

Supplementary Data are available at NAR Online.

ACKNOWLEDGEMENTS

We gratefully acknowledge T. Jenuwein (*Suv39h1/2* and *Suv4-20h1/2* dn ESCs, HP1α/β plasmids), G. Schotta (*Suv4-20h1/2* dn ESCs), M. Bühler (*Adnp* ko ESCs), K. Rippe (pGFP-NPM plamid), J. Betschinger (pPy-CAG-CreERT2 plasmid), C. Cepko (pCAG-Cre:GFP plasmid) for providing reagents. We thank L. Gelman, L. Plantard and J. Eglinger (Facility for Advanced Imaging and Microscopy), H. Kohler (Cell Sorting), S. Smallwood (Functional genomics) and members of the FMI animal facility for excellent assistance. We thank L. Pelloni for assistance with ESC culture.

Author contributions: M.T. and A.H.F.M.P. conceived the study. D.B., M.T., G.F. and A.H.F.M.P. designed the experiments and interpreted the data. M.T. generated and characterized HP1α/β mutant and control ESC lines and performed imaging experiments. D.B. carried out molecular biology, imaging, cell cycle & sorting experiments. A.G.M. and C.G. performed electron microscopy experiments. R.O. and D.B. analyzed imaging data. E.A.O. performed RNA-seq analyses. G.F. and A.H.F.M.P. supervised the project. D.B., G.F. and A.H.F.M.P. wrote the manuscript with input from all authors.

FUNDING

Novartis Research Foundation; Swiss National Science Foundation [31003A-172873]; European Research Council (ERC) under the European Union's Horizon 2020 research and innovation programme [ERC-AdG 695288 - Totipotency]. Funding for open access charge: European Research Council (ERC) [ERC-AdG 695288 - Totipotency].

Conflict of interest statement. None declared.

REFERENCES

1. Azkanaz,M., López,A.R., de Boer,B., Huiting,W., Angrand,P.O., Vellenga,E., Kampinga,H.H., Bergink,S., Martens,J.H.A., Schuringa,J.J. *et al.* (2019) Protein quality control in the nucleolus safeguards recovery of epigenetic regulators after heat shock. *Elife.*, **8**, e45205.
2. Boulon,S., Westman,B.J., Hutten,S., Boisvert,F.M. and Lamond,A.I. (2010) The Nucleolus under Stress. *Mol. Cell.*, **40**, 216–227.
3. Frottin,F., Schueder,F., Tiwary,S., Gupta,R., Körner,R., Schlichthaerle,T., Cox,J., Jungmann,R., Hartl,F.U. and Hipp,M.S. (2019) The nucleolus functions as a phase-separated protein quality control compartment. *Science*, **365**, 342–347.
4. James,A., Wang,Y., Raje,H., Rosby,R. and DiMario,P. (2014) Nucleolar stress with and without p53. *Nucleus*, **5**, 402–426.
5. Pfister,A.S. (2019) Emerging role of the nucleolar stress response in autophagy. *Front. Cell. Neurosci.*, **13**, 156.
6. Tsai,R.Y.L. and Pederson,T. (2014) Connecting the nucleolus to the cell cycle and human disease. *FASEB J.*, **28**, 3290–3296.

7. Farley-Barnes,K.I., Ogawa,L.M. and Baserga,S.J. (2019) Ribosomopathies: old concepts, new controversies. *Trends Genet.*, **35**, 754.
8. Latonen,L. (2019) Phase-to-phase with nucleoli – stress responses, protein aggregation and novel roles of RNA. *Front Cell. Neurosci.*, **13**, 151.
9. Dev,V.G., Tantravahi,R., Miller,D.A. and Miller,O.J. (1977) Nucleolus organizers in MUS MUSCULUS subspecies and in the Rag mouse cell line. *Genetics*, **86**, 389.
10. Kurihara,Y., Suh,D.S., Suzuki,H. and Moriwaki,K. (1994) Chromosomal locations of Ag-NORs and clusters of ribosomal DNA in laboratory strains of mice. *Mamm. Genome*, **5**, 225–228.
11. Savino,T.M., Gébrane-Younès,J., de Mey,J., Sibarita,J.B. and Hernandez-Verdun, D. (2001) Nucleolar assembly of the rRNA processing machinery in living cells. *J. Cell. Biol.*, **153**, 1097–1110.
12. Muro,E., Gébrane-Younès,J., Jobart-Malfait,A., Louvet,E., Roussel,P. and Hernandez-Verdun,D. (2010) The traffic of proteins between nucleolar organizer regions and prenucleolar bodies governs the assembly of the nucleolus at exit of mitosis. *Nucleus*, **1**, 202–211.
13. Hernandez-Verdun,D. (2011) Assembly and disassembly of the nucleolus during the cell cycle. *Nucleus*, **2**, 189–194.
14. Boisvert,F.M., van Koningsbruggen,S., Navascués,J. and Lamond,A.I. (2007) The multifunctional nucleolus. *Nat. Rev. Mol. Cell. Biol.*, **8**, 574–585.
15. Lafontaine,D.L.J., Riback,J.A., Bascetin,R. and Brangwynne,C.P. (2021) The nucleolus as a multiphase liquid condensate. *Nat. Rev. Mol. Cell. Biol.*, **22**, 165–182.
16. Mitrea,D.M., Cika,J.A., Stanley,C.B., Nourse,A., Onuchic,P.L., Banerjee,P.R., Phillips,A.H., Park,C.G., Deniz,A.A. and Kriwacki,R.W. (2018) Self-interaction of NPM1 modulates multiple mechanisms of liquid-liquid phase separation. *Nat. Commun.*, **9**, 842.
17. Mitrea,D.M., Cika,J.A., Guy,C.S., Ban,D., Banerjee,P.R., Stanley,C.B., Nourse,A., Deniz,A.A. and Kriwacki,R.W. (2016) Nucleophosmin integrates within the nucleolus via multi-modal interactions with proteins displaying R-rich linear motifs and rRNA. *Elife.*, **5**, e13571.
18. Feric,M., Vaidya,N., Harmon,T.S., Mitrea,D.M., Zhu,L., Richardson,T.M., Kriwacki,R.W., Pappu,R.v. and Brangwynne,C.P. (2016) Coexisting Liquid Phases Underlie Nucleolar Subcompartments. *Cell*, **165**, 1686–1697.
19. Kampen,K.R., Sulima,S.O., Vereecke,S. and de Keersmaecker,K. (2020) Hallmarks of ribosomopathies. *Nucleic Acids Res.*, **48**, 1013–1028.
20. Correll,C.C., Bartek,J. and Dundr,M. (2019) The nucleolus: a multiphase condensate balancing ribosome synthesis and translational capacity in health, aging and ribosomopathies. *Cells*, **8**, 869.
21. Stochaj,U. and Weber,S.C. (2020) Nucleolar organization and functions in health and disease. *Cells*, **9**, 526.
22. Kang,J., Brajanovski,N., Chan,K.T., Xuan,J., Pearson,R.B. and Sanij,E. (2021) Ribosomal proteins and human diseases: molecular mechanisms and targeted therapy. *Signal Transduct. Targeted Ther.*, **6**, 1–22.
23. Stamatopoulou,V., Parisot,P., de Vleeschouwer,C. and Lafontaine,D.L.J. (2018) Use of the iNo score to discriminate normal from altered nucleolar morphology, with applications in basic cell biology and potential in human disease diagnostics. *Nat. Protoc.*, **13**, 2387–2406.
24. Guzman-Ayala,M., Sachs,M., Koh,F.M., Onodera,C., Bulut-Karslioglu,A., Lin,C.J., Wong,P., Nitta,R., Song,J.S. and Ramalho-Santos,M. (2015) Chd1 is essential for the high transcriptional output and rapid growth of the mouse epiblast. *Development (Cambridge)*, **142**, 118–127.
25. Meshorer,E. and Misteli,T. (2006) Chromatin in pluripotent embryonic stem cells and differentiation. *Nat. Rev. Mol. Cell. Biol.*, **7**, 540–546.
26. Schlesinger,S., Selig,S., Bergman,Y. and Cedar,H. (2009) Allelic inactivation of rDNA loci. *Genes Dev.*, **23**, 2437.
27. Savić,N., Bär,D., Leone,S., Frommel,S.C., Weber,F.A., Vollenweider,E., Ferrari,E., Ziegler,U., Kaech,A., Shakhova,O. *et al.* (2014) lncRNA maturation to initiate heterochromatin formation in the nucleolus is required for exit from pluripotency in ESCs. *Cell. Stem. Cell.*, **15**, 720–734.
28. Leone,S., Bär,D., Slabber,C.F., Dalcher,D. and Santoro,R. (2017) The RNA helicase DHX9 establishes nucleolar heterochromatin, and this activity is required for embryonic stem cell differentiation. *EMBO Rep.*, **18**, 1248–1262.
29. Bhattacharya,D., Talwar,S., Mazumder,A. and Shivashankar,G.v. (2009) Spatio-temporal plasticity in chromatin organization in mouse cell differentiation and during Drosophila embryogenesis. *Biophys. J.*, **96**, 3832–3839.
30. Bártová,E., Krejčí,J., Harničarová,A. and Kozubek,S. (2008) Differentiation of human embryonic stem cells induces condensation of chromosome territories and formation of heterochromatin protein 1 foci. *Differentiation*, **76**, 24–32.
31. Wiblin,A.E., Cui,W., Clark,J.A. and Bickmore,W.A. (2005) Distinctive nuclear organisation of centromeres and regions involved in pluripotency in human embryonic stem cells. *J. Cell. Sci.*, **118**, 3861–3868.
32. Vissel,B. and Choo,K.H. (1989) Mouse major (gamma) satellite DNA is highly conserved and organized into extremely long tandem arrays: implications for recombination between nonhomologous chromosomes. *Genomics*, **5**, 407–414.
33. Rea,S., Eisenhaber,F., O'Carroll,D., Strahl,B.D., Sun,Z.W., Schmid,M., Opravil,S., Mechtier,K., Ponting,C.P., Allis,C.D. *et al.* (2000) Regulation of chromatin structure by site-specific histone H3 methyltransferases. *Nature*, **406**, 593–599.
34. Peters,A.H.F.M., O'Carroll,D., Scherthan,H., Mechtler,K., Sauer,S., Schöfer,C., Weipoltshammer,K., Pagani,M., Lachner,M., Kohlmaier,A. *et al.* (2001) Loss of the Suv39h histone methyltransferases impairs mammalian heterochromatin and genome stability. *Cell*, **107**, 323–337.
35. Bannister,A.J., Zegerman,P., Partridge,J.F., Miska,E.A., Thomas,J.O., Allshire,R.C. and Kouzarides,T. (2001) Selective recognition of methylated lysine 9 on histone H3 by the HP1 chromo domain. *Nature*, **410**, 120–124.
36. Lachner,M., O'Carroll,D., Rea,S., Mechtler,K. and Jenuwein,T. (2001) Methylation of histone H3 lysine 9 creates a binding site for HP1 proteins. *Nature*, **410**, 116–120.
37. Stewart,M.D., Li,J. and Wong,J. (2005) Relationship between histone H3 lysine 9 methylation, transcription repression, and heterochromatin protein 1 recruitment. *Mol. Cell. Biol.*, **25**, 2525.
38. Yamamoto,K. and Sonoda,M. (2003) Self-interaction of heterochromatin protein 1 is required for direct binding to histone methyltransferase, SUV39H1. *Biochem. Biophys. Res. Commun.*, **301**, 287–292.
39. Aagaard,L., Laible,G., Selenko,P., Schmid,M., Dorn,R., Schotta,G., Kuhfittig,S., Wolf,A., Lebersorger,A., Singh,P.B. *et al.* (1999) Functional mammalian homologues of the Drosophila PEV-modifier Su(var)3-9 encode centromere-associated proteins which complex with the heterochromatin component M31. *EMBO J.*, **18**, 1923–1938.
40. Muramatsu,D., Singh,P.B., Kimura,H., Tachibana,M. and Shinkai,Y. (2013) Pericentric heterochromatin generated by HP1 protein interaction-defective histone methyltransferase Suv39h1. *J. Biol. Chem.*, **288**, 25285–25296.
41. Thiru,A., Nietlispach,D., Mott,H.R., Okuwaki,M., Lyon,D., Nielsen,P.R., Hirshberg,M., Verreault,A., Murzina,N.v. and Laue,E.D. (2004) Structural basis of HP1/PXVXL motif peptide interactions and HP1 localisation to heterochromatin. *EMBO J.*, **23**, 489–499.
42. Hiragami-Hamada,K., Soeroes,S., Nikolov,M., Wilkins,B., Kreuz,S., Chen,C., de La Rosa-Velázquez,I.A., Zenn,H.M. and Kost,N. (2016) Dynamic and flexible H3K9me3 bridging via HP1β dimerization establishes a plastic state of condensed chromatin. *Nat. Commun.*, **7**, 11310.
43. Hahn,M., Dambacher,S., Dulev,S., Kuznetsova,A.Y., Eck,S., Wörz,S., Sadic,D., Schulte,M., Mallm,J.P., Maiser,A. *et al.* (2013) Suv4-20h2 mediates chromatin compaction and is important for cohesin recruitment to heterochromatin. *Genes Dev.*, **27**, 859–872.
44. Lehnertz,B., Ueda,Y., Derijck,A.A.H.A., Braunschweig,U., Perez-Burgos,L., Kubicek,S., Chen,T., Li,E., Jenuwein,T. and Peters,A.H.F.M. (2003) Suv39h-mediated histone H3 lysine 9 methylation directs DNA methylation to major satellite repeats at pericentric heterochromatin. *Curr. Biol.*, **13**, 1192–1200.
45. Lechner,M.S., Begg,G.E., Speicher,D.W. and Rauscher,F.J. (2000) Molecular determinants for targeting heterochromatin protein

1-mediated gene silencing: direct chromoshadow domain-KAP-1 corepressor interaction is essential. *Mol. Cell. Biol.*, **20**, 6449–6465.
46. Brasher,S.v., Smith,B.O., Fogh,R.H., Nietlispach,D., Thiru,A., Nielsen,P.R., Broadhurst,R.W., Ball,L.J., Murzina,N.v. and Laue,E.D. (2000) The structure of mouse HP1 suggests a unique mode of single peptide recognition by the shadow chromo domain dimer. *EMBO J.*, **19**, 1587–1597.
47. Strickfaden,H., Tolsma,T.O., Sharma,A., Underhill,D.A., Hansen,J.C. and Hendzel,M.J. (2020) Condensed Chromatin Behaves like a Solid on the Mesoscale In Vitro and in Living Cells. *Cell*, **183**, 1772–1784.
48. Erdel,F., Rademacher,A., Vlijm,R., Herten,D.-P., Engelhardt,J. and Correspondence,K.R. (2020) Mouse Heterochromatin Adopts Digital Compaction States without Showing Hallmarks of HP1-Driven Liquid-Liquid Phase Separation. *Mol. Cell.*, **78**, 236–248.
49. Cheutin,T., McNairn,A.J., Jenuwein,T., Gilbert,D.M., Singh,P.B. and Misteli,T. (2003) Maintenance of stable heterochromatin domains by dynamic HP1 binding. *Science*, **299**, 721–725.
50. Schmiedeberg,L., Weisshart,K., Diekmann,S., Hoerste,G.M.Z. and Hemmerich,P. (2004) High- and Low-mobility Populations of HP1 in Heterochromatin of Mammalian Cells. *Mol. Biol. Cell.*, **15**, 2819.
51. Souza,P.P., Völkel,P., Trinel,D., Vandamme,J., Rosnoblet,C., Héliot,L. and Angrand,P.O. (2009) The histone methyltransferase SUV420H2 and Heterochromatin Proteins HP1 interact but show different dynamic behaviours. *BMC Cell. Biol.*, **10**, 41.
52. Keenen,M.M., Brown,D., Brennan,L.D., Renger,R., Khoo,H., Carlson,C.R., Huang,B., Grill,S.W., Narlikar,G.J. and Redding,S. (2021) HP1 proteins compact dna into mechanically and positionally stable phase separated domains. *Elife.*, **10**, e64563.
53. Larson,A.G., Elnatan,D., Keenen,M.M., Trnka,M.J., Johnston,J.B., Burlingame,A.L., Agard,D.A., Redding,S. and Narlikar,G.J. (2017) Liquid droplet formation by HP1α suggests a role for phase separation in heterochromatin. *Nature*, **547**, 236–240.
54. Strom,A.R., Emelyanov,A.v., Mir,M., Fyodorov,D.v., Darzacq,X. and Karpen,G.H. (2017) Phase separation drives heterochromatin domain formation. *Nature*, **547**, 241–245.
55. Sanulli,S., Trnka,M.J., Dharmarajan,V., Tibble,R.W., Pascal,B.D., Burlingame,A.L., Griffin,P.R., Gross,J.D. and Narlikar,G.J. (2019) HP1 reshapes nucleosome core to promote phase separation of heterochromatin. *Nature*, **575**, 390–394.
56. Wang,L., Gao,Y., Zheng,X., Liu,C., Dong,S., Li,R., Zhang,G., Wei,Y., Qu,H., Li,Y. *et al.* (2019) Histone Modifications Regulate Chromatin Compartmentalization by Contributing to a Phase Separation Mechanism. *Mol. Cell.*, **76**, 646–659.
57. Aagaard,L., Laible,G., Selenko,P., Schmid,M., Dorn,R., Schotta,G., Kuhfittig,S., Wolf,A., Lebersorger,A., Singh,P.B. *et al.* (1999) Functional mammalian homologues of the Drosophila PEV-modifier Su(var)3-9 encode centromere-associated proteins which complex with the heterochromatin component M31. *EMBO J.*, **18**, 1923.
58. Ekwall,K., Javerzat,J.P., Lorentz,A., Schmidt,H., Cranston,G. and Allshire,R. (1995) The chromodomain protein Swi6: A key component at fission yeast centromeres. *Science*, **269**, 1429–1431.
59. Ekwall,K., Nimmo,E.R., Javerzat,J.P., Borgstrøm,B., Egel,R., Cranston,G. and Allshire,R. (1996) Mutations in the fission yeast silencing factors clr4+ and rik1+ disrupt the localisation of the chromo domain protein Swi6p and impair centromere function. *J. Cell. Sci.*, **109**(Pt 11), 2637–2648.
60. Montavon,T., Shukeir,N., Erikson,G., Engist,B., Onishi-Seebacher,M., Ryan,D., Musa,Y., Mittler,G., Meyer,A.G., Genoud,C. *et al.* (2021) Complete loss of H3K9 methylation dissolves mouse heterochromatin organization. *Nat. Commun.*, **12**, 4359.
61. Németh,A. and Längst,G. (2011) Genome organization in and around the nucleolus. *Trends Genet.*, **27**, 149–156.
62. Towbin,B.D., Gonzalez-Sandoval,A. and Gasser,S.M. (2013) Mechanisms of heterochromatin subnuclear localization. *Trends Biochem. Sci.*, **38**, 356–363.
63. Padeken,J. and Heun,P. (2014) Nucleolus and nuclear periphery: velcro for heterochromatin. *Curr. Opin. Cell. Biol.*, **28**, 54–60.
64. Conrad,N.K., Shu,M.di, Uyhazi,K.E. and Steitz,J.A. (2007) Mutational analysis of a viral RNA element that counteracts rapid RNA decay by interaction with the polyadenylate tail. *Proc. Natl. Acad. Sci. U.S.A.*, **104**, 10412–10417.
65. Tardat,M., Albert,M., Kunzmann,R., Liu,Z., Kaustov,L., Thierry,R., Duan,S., Brykczynska,U., Arrowsmith,C.H. and Peters,A.H.F.M. (2015) Cbx2 targets PRC1 to constitutive heterochromatin in mouse zygotes in a parent-of-origin-dependent manner. *Mol. Cell.*, **58**, 157–171.
66. Schotta,G., Sengupta,R., Kubicek,S., Malin,S., Kauer,M., Callén,E., Celeste,A., Pagani,M., Opravil,S. and de La Rosa-Velazquez,I.A. (2008) A chromatin-wide transition to H4K20 monomethylation impairs genome integrity and programmed DNA rearrangements in the mouse. *Genes Dev.*, **22**, 2048.
67. Ostapcuk,V., Mohn,F., Carl,S.H., Basters,A., Hess,D., Iesmantavicius,V., Lampersberger,L., Flemr,M., Pandey,A., Thomä,N.H. *et al.* (2018) Activity-dependent neuroprotective protein recruits HP1 and CHD4 to control lineage-specifying genes. *Nature*, **557**, 739–743.
68. Koulen,P., Fletcher,E.L., Craven,S.E., Bredt,D.S. and Wässle,H. (1998) Immunocytochemical localization of the postsynaptic density protein PSD-95 in the mammalian retina. *J. Neurosci.*, **18**, 10136–10149.
69. Gopal,S., Chiappini,C., Armstrong,J.P.K., Chen,Q., Serio,A., Hsu,C.C., Meinert,C., Klein,T.J., Hutmacher,D.W., Rothery,S. *et al.* (2019) Immunogold FIB-SEM: combining volumetric ultrastructure visualization with 3D biomolecular analysis to dissect cell-environment interactions. *Adv. Mater.*, **31**, e1900488.
70. Weigert,M., Schmidt,U., Boothe,T., Müller,A., Dibrov,A., Jain,A., Wilhelm,B., Schmidt,D., Broaddus,C., Culley,S. *et al.* (2018) Content-aware image restoration: pushing the limits of fluorescence microscopy. *Nat. Methods*, **15**, 1090–1097.
71. Li,C.H. and Tam,P.K.S. (1998) An iterative algorithm for minimum cross entropy thresholding. *Pattern Recognit. Lett.*, **19**, 771–776.
72. Otsu,N. (1979) Threshold selection method from gray-level histograms. *IEEE Trans. Syst. Man. Cybern.*, **9**, 62–66.
73. Bradski,G. (2000) The OpenCV Library. In: *Dr. Dobb's Journal of Software Tools*.
74. Ronneberger,O., Fischer,P. and Brox,T. (2015) U-Net: Convolutional Networks for Biomedical Image Segmentation. *Lect. Notes Comput. Sci.*, **9351**, 234–241.
75. Minc,E., Allory,Y., Worman,H.J., Courvalin,J.C. and Buendia,B. (1999) Localization and phosphorylation of HP1 proteins during the cell cycle in mammalian cells. *Chromosoma*, **108**, 220–234.
76. Smothers,J.F. and Henikoff,S. (2001) The hinge and chromo shadow domain impart distinct targeting of HP1-like proteins. *Mol. Cell. Biol.*, **21**, 2555–2569.
77. Canzio,D., Larson,A. and Narlikar,G.J. (2014) Mechanisms of functional promiscuity by HP1 proteins. *Trends Cell. Biol.*, **24**, 377–386.
78. Horsley,D., Hutchings,A., Butcher,G.W. and Singh,P.B. (1996) M32, a murine homologue of Drosophila heterochromatin protein 1 (HP1), localises to euchromatin within interphase nuclei and is largely excluded from constitutive heterochromatin. *Cytogenet. Cell. Genet.*, **73**, 308–311.
79. Guenatri,M., Bailly,D., Maison,C. and Almouzni,G. (2004) Mouse centric and pericentric satellite repeats form distinct functional heterochromatin. *J. Cell. Biol.*, **166**, 493–505.
80. Dialynas,G.K., Terjung,S., Brown,J.P., Aucott,R.L., Baron-Luhr,B., Singh,P.B. and Georgatos,S.D. (2007) Plasticity of HP1 proteins in mammalian cells. *J. Cell. Sci.*, **120**, 3415–3424.
81. Bosch-Presegué,L., Raurell-Vila,H., Thackray,J.K., González,J., Casal,C., Kane-Goldsmith,N., Vizoso,M., Brown,J.P., Gómez,A., Ausió,J. *et al.* (2017) Mammalian HP1 Isoforms Have Specific Roles in Heterochromatin Structure and Organization. *Cell Rep.*, **21**, 2048–2057.
82. Peters,A.H.F.M., Kubicek,S., Mechtler,K., O'Sullivan,R.J., Derijck,A.A.H.A., Perez-Burgos,L., Kohlmaier,A., Opravil,S., Tachibana,M., Shinkai,Y. *et al.* (2003) Partitioning and plasticity of repressive histone methylation states in mammalian chromatin. *Mol. Cell.*, **12**, 1577–1589.
83. Schotta,G., Lachner,M., Sarma,K., Ebert,A., Sengupta,R., Reuter,G., Reinberg,D. and Jenuwein,T. (2004) A silencing pathway to induce H3-K9 and H4-K20 trimethylation at constitutive heterochromatin. *Genes Dev.*, **18**, 1251–1262.

84. Raurell-Vila,H., Bosch-Presegue,L., Gonzalez,J., Kane-Goldsmith,N., Casal,C., Brown,J.P., Marazuela-Duque,A., Singh,P.B., Serrano,L. and Vaquero,A. (2017) An HP1 isoform-specific feedback mechanism regulates Suv39h1 activity under stress conditions. *Epigenetics*, **12**, 166–175.
85. Efroni,S., Duttagupta,R., Cheng,J., Dehghani,H., Hoeppner,D.J., Dash,C., Bazett-Jones,D.P., le Grice,S., McKay,R.D.G., Buetow,K.H. *et al.* (2008) Global transcription in pluripotent embryonic stem cells. *Cell. Stem. Cell.*, **2**, 437–447.
86. Ahmed,K., Dehghani,H., Rugg-Gunn,P., Fussner,E., Rossant,J. and Bazett-Jones,D.P. (2010) Global chromatin architecture reflects pluripotency and lineage commitment in the early mouse embryo. *PLoS One*, **5**, e10531.
87. Yuan,X., Zhou,Y., Casanova,E., Chai,M., Kiss,E., Gröne,H.J., Schütz,G. and Grummt,I. (2005) Genetic inactivation of the transcription factor TIF-IA leads to nucleolar disruption, cell cycle arrest, and p53-mediated apoptosis. *Mol. Cell.*, **19**, 77–87.
88. Ugrinova,I., Monier,K., Ivaldi,C., Thiry,M., Storck,S., Mongelard,F. and Bouvet,P. (2007) Inactivation of nucleolin leads to nucleolar disruption, cell cycle arrest and defects in centrosome duplication. *BMC Mol. Biol.*, **8**, 66.
89. Nicolas,E., Parisot,P., Pinto-Monteiro,C., de Walque,R., de Vleeschouwer,C. and Lafontaine,D.L.J. (2016) Involvement of human ribosomal proteins in nucleolar structure and p53-dependent nucleolar stress. *Nat. Commun.*, **7**, 11390.
90. Tiku,V., Jain,C., Raz,Y., Nakamura,S., Heestand,B., Liu,W., Späth,M., Suchiman,H.E.D., Müller,R.U., Slagboom,P.E. *et al.* (2017) Small nucleoli are a cellular hallmark of longevity. *Nat. Commun.*, **8**, 16083.
91. Rosnoblet,C., Vandamme,J., Völkel,P. and Angrand,P.O. (2011) Analysis of the human HP1 interactome reveals novel binding partners. *Biochem. Biophys. Res. Commun.*, **413**, 206–211.
92. Mattout,A., Aaronson,Y., Sailaja,B.S., Raghu Ram,E.v., Harikumar,A., Mallm,J.P., Sim,K.H., Nissim-Rafinia,M., Supper,E., Singh,P.B. *et al.* (2015) Heterochromatin Protein 1β (HP1β) has distinct functions and distinct nuclear distribution in pluripotent versus differentiated cells. *Genome Biol.*, **16**, 213.
93. Martens,J.H.A., O'Sullivan,R.J., Braunschweig,U., Opravil,S., Radolf,M., Steinlein,P. and Jenuwein,T. (2005) The profile of repeat-associated histone lysine methylation states in the mouse epigenome. *EMBO J.*, **24**, 800.
94. Lu,J. and Gilbert,D.M. (2007) Proliferation-dependent and cell cycle regulated transcription of mouse pericentric heterochromatin. *J. Cell. Biol.*, **179**, 411–421.
95. Suso Platero,J., Hartnett,T. and Eissenberg,J.C. (1995) Functional analysis of the chromo domain of HP1. *EMBO J.*, **14**, 3977.
96. Maeda,R. and Tachibana,M. (2022) HP1 maintains protein stability of H3K9 methyltransferases and demethylases. *EMBO Rep.*, **23**, e53581.
97. Murzina,N., Verreault,A., Laue,E. and Stillman,B. (1999) Heterochromatin dynamics in mouse cells: interaction between chromatin assembly factor 1 and HP1 proteins. *Mol. Cell.*, **4**, 529–540.
98. Quivy,J.P., Roche,D., Kirschner,D., Tagami,H., Nakatani,Y. and Almouzni,G. (2004) A CAF-1 dependent pool of HP1 during heterochromatin duplication. *EMBO J.*, **23**, 3516–3526.
99. Müller-Ott,K., Erdel,F., Matveeva,A., Mallm,J.-P., Rademacher,A., Hahn,M., Bauer,C., Zhang,Q., Kaltofen,S., Schotta,G. *et al.* (2014) Specificity, propagation, and memory of pericentric heterochromatin. *Mol. Syst. Biol.*, **10**, 746.
100. Kaaij,L.J.T., Mohn,F., van der Weide,R.H., de Wit,E. and Bühler,M. (2019) The ChAHP Complex Counteracts Chromatin Looping at CTCF Sites that Emerged from SINE Expansions in Mouse. *Cell*, **178**, 1437–1451.
101. Bulut-Karslioglu,A., DeLaRosa-Velázquez,I.A., Ramirez,F., Barenboim,M., Onishi-Seebacher,M., Arand,J., Galán,C., Winter,G.E., Engist,B., Gerle,B. *et al.* (2014) Suv39h-dependent H3K9me3 marks intact retrotransposons and silences LINE elements in mouse embryonic stem cells. *Mol. Cell.*, **55**, 277–290.
102. Mills,E.W. and Green,R. (2017) Ribosomopathies: there's strength in numbers. *Science*, **358**, eaan2755.
103. Papagiannopoulos,C.I., Kyritsis,K.A., Psatha,K., Mavridou,D., Chatzopoulou,F., Orfanoudaki,G., Aivaliotis,M. and Vizirianakis,I.S. (2022) Invariable ribosome stoichiometry during murine erythroid differentiation: implications for understanding ribosomopathies. *Front Mol. Biosci.*, **9**, 30.
104. Voit,R. and Grummt,I. (2001) Phosphorylation of UBF at serine 388 is required for interaction with RNA polymerase I and activation of rDNA transcription. *Proc. Natl. Acad. Sci. U.S.A.*, **98**, 13631–13636.
105. Peng,J.C. and Karpen,G.H. (2007) H3K9 methylation and RNA interference regulate nucleolar organization and repeated DNA stability. *Nat. Cell. Biol.*, **9**, 25–35.
106. Strom,A.R., Biggs,R.J., Banigan,E.J., Wang,X., Chiu,K., Herman,C., Collado,J., Yue,F., Politz,J.C.R., Tait,L.J. *et al.* (2021) Hp1α is a chromatin crosslinker that controls nuclear and mitotic chromosome mechanics. *Elife.*, **10**, e63972.
107. Stephens,A.D., Liu,P.Z., Kandula,V., Chen,H., Almassalha,L.M., Herman,C., Backman,V., O'Halloran,T., Adam,S.A., Goldman,R.D. *et al.* (2019) Physicochemical mechanotransduction alters nuclear shape and mechanics via heterochromatin formation. *Mol. Biol. Cell.*, **30**, 2320–2330.
108. Zhou,H., Li,L., Wang,Q., Hu,Y., Zhao,W., Gautam,M. and Li,L. (2020) H3K9 demethylation-induced R-loop accumulation is linked to disorganized nucleoli. *Front. Genet.*, **11**, 43.
109. Yuan,X., Feng,W., Imhof,A., Grummt,I. and Zhou,Y. (2007) Activation of RNA polymerase I transcription by cockayne syndrome group B protein and histone methyltransferase G9a. *Mol. Cell.*, **27**, 585–595.
110. Derenzini,M., Trerè,D., Pession,A., Montanaro,L., Sirri,V. and Ochs,R.L. (1998) Nucleolar function and size in cancer cells. *Am. J. Pathol.*, **152**, 1291.
111. Moss,T., Mars,J.C., Tremblay,M.G. and Sabourin-Felix,M. (2019) The chromatin landscape of the ribosomal RNA genes in mouse and human. *Chromosome Res.*, **27**, 31–40.
112. Diesch,J., Bywater,M.J., Sanij,E., Cameron,D.P., Schierding,W., Brajanovski,N., Son,J., Sornkom,J., Hein,N., Evers,M. *et al.* (2019) Changes in long-range rDNA-genomic interactions associate with altered RNA polymerase II gene programs during malignant transformation. *Commun. Biol.*, **2**, 39.
113. Hayashi,Y., Kuroda,T., Kishimoto,H., Wang,C., Iwama,A. and Kimura,K. (2014) Downregulation of rRNA transcription triggers cell differentiation. *PLoS One*, **9**, e98586.
114. Kononowicz,H. and Janick,J. (1988) Changes in nucleus, nucleolus and cell size accompanying somatic embryogenesis of Theobroma cacao L. I. Relationship between DNA and total protein content and size of nucleus, nucleolus and cell. *Folia Histochem. Cytobiol.*, **26**, 237–247.
115. Mukherjee,R.N., Chen,P. and Levy,D.L. (2016) Recent advances in understanding nuclear size and shape. *Nucleus*, **7**, 167–186.
116. Narla,A. and Ebert,B.L. (2010) Ribosomopathies: human disorders of ribosome dysfunction. *Blood*, **115**, 3196–3205.
117. Shiratori,M., Suzuki,T., Itoh,C., Goto,M., Furuichi,Y. and Matsumoto,T. (2002) WRN helicase accelerates the transcription of ribosomal RNA as a component of an RNA polymerase I-associated complex. *Oncogene*, **21**, 2447–2454.
118. Shiratori,M., Suzuki,T., Itoh,C., Goto,M., Furuichi,Y. and Matsumoto,T. (2002) WRN helicase accelerates the transcription of ribosomal RNA as a component of an RNA polymerase I-associated complex. *Oncogene.*, **21**, 2447–2454.
119. Karikkineth,A.C., Scheibye-Knudsen,M., Fivenson,E., Croteau,D.L. and Bohr,V.A. (2017) Cockayne syndrome: Clinical features, model systems and pathways. *Ageing. Res. Rev.*, **33**, 3–17.
120. Hernández-Ortega,K., Garcia-Esparcia,P., Gil,L., Lucas,J.J. and Ferrer,I. (2016) Altered Machinery of Protein Synthesis in Alzheimer's: From the Nucleolus to the Ribosome. *Brain Pathol.*, **26**, 593–605.
121. Zhang,W., Li,J., Suzuki,K., Qu,J., Wang,P., Zhou,J., Liu,X., Ren,R., Xu,X., Ocampo,A. *et al.* (2015) A Werner syndrome stem cell model unveils heterochromatin alterations as a driver of human aging. *Science*, **348**, 1160.
122. Lee,J.H., Demarest,T.G., Babbar,M., Kim,E.W., Okur,M.N., De,S., Croteau,D.L. and Bohr,V.A. (2019) Cockayne syndrome group B deficiency reduces H3K9me3 chromatin remodeler SETDB1 and exacerbates cellular aging. *Nucleic Acids Res.*, **47**, 8548–8562.
123. Tsurumi,A. and Li,W.X. (2012) Global heterochromatin loss: a unifying theory of aging?*Epigenetics*, **7**, 680–688.

124. Oberdoerffer,P. and Sinclair,D.A. (2007) The role of nuclear architecture in genomic instability and ageing. *Nat. Rev. Mol. Cell. Biol.*, **8**, 692–702.
125. López-Otín,C., Blasco,M.A., Partridge,L., Serrano,M. and Kroemer,G. (2013) The hallmarks of aging. *Cell*, **153**, 1194–1217.
126. Lee,J.H., Kim,E.W., Croteau,D.L. and Bohr,V.A. (2020) Heterochromatin: an epigenetic point of view in aging. *Exp. Mol. Med.*, **52**, 1466–1474.